TECHNISCHE UNIVERSITÄT WIEN

CERN

Master Thesis

X-ray Interferometry with the Heterodyne Nearfield Speckles Technique for Beam Size Monitoring at FCC-ee

carried out for the purpose of obtaining the degree of Master of Science,
submitted at TU Wien, Faculty of Atominstitut

Alexander Götz, BSc
Mat.Nr.: 01525657

under the supervision of

Privatdoz. Dipl.-Ing. Dr.techn. Michael Benedikt
Atominstitut, E141

1 Abstract

By recording the interference pattern between X-ray synchrotron radiation emitted by an electron beam and the tiny portion of radiation scattered by a stochastic distribution of nanoparticles, one can measure the first-order transverse coherence of the radiation. Under the conditions of applicability of the Van Cittert and Zernike theorem, the spatial coherence is linked to the transverse intensity distribution of the source, which can be used for beam diagnostics at the projected Future Circular Lepton Collider at CERN.

In this work, the method is evaluated theoretically and is furthermore tested by simulating the production of the synchrotron radiation and its propagation through the involved optical elements. The method is then shown to be capable for determining the transverse beam size of the Future Circular Lepton Collider on a bunch-per-bunch basis and to be feasible with today's technology.

Contents

2 Summary

First described in 2001 [1][2], Heterodyne Nearfield Speckles is a well probed technique for the measurement of size of nano and microparticles, often referred to as colloids. Its principles rely on the interference of a strong transmitted photon beam and many relatively week scattered beams. By analysing the shape of the coherence areas (speckles), using a fully coherent laser beam, one can deduct the scattering amplitude function and as a consequence the size of the observed colloids.

Reversing this measurement by using colloids of a known size and a radiation of an unknown partial coherence, it is possible to determine the coherence properties and therefore the spectrum and the size of the initial photon beam at the emission plane. The radiation used for this purpose is the synchrotron radiation, which is emitted by relativistic electrons passing through the magnetic structures of accelerators. This has been shown for an undulator at the European Synchrotron Radiation Facility (ESRF) in Grenoble in 2009 [3], at ALBA-CELLS in Cerdanyola del Vallès (Barcelona), in 2017 [4] and in 2019 [5].

Adapting this non invasive technique of measuring the beam size to a bending magnet at the Future Circular Lepton Collider (FCC-ee) raises several challenges. This includes the difficulties of a monochromator for hard X-ray, the small refractive index of the colloids for X-ray and the conversion to visible light and finally the optimising of the parameters being constrained by the machine design.

This thesis is going to deal with those challenges in three steps. First, the measurement is modelled theoretically to find an optimal set of parameters. Secondly, this technique is simulated numerically, to see whether certain approximations hold true for the given magnetic structure, the propagation of the beam and the scattering of the particles [1]. Thirdly, the optical transfer function is measured experimentally, to see whether beam size monitoring is possible with a certain optical setup.

[1] All codes used in this thesis can be found at `https://github.com/ajg4/speckles`

3 Introduction to FCC-ee

3.1 Physical Discovery Potential

In 2013 the European Strategy for Particle Physics Update stated that Europe needs to be in a position to propose an ambitious post-Large Hadron Collider (LHC) accelerator project at CERN, to stay at the forefront of particle physics. Further pursuing its core mission, to elucidate the laws of nature at most fundamental level, it was a consequent demand to undertake design studies for accelerator projects in a global context. Under these circumstances the Future Circular Collider (FCC) study was launched, whose physical discovery potential should serve the world wide particle-physics community throughout the 21st century [6].

As a part of these studies, a design report of a highest-luminosity energy frontier electron-positron collider (FCC-ee) was published targeting open questions of modern physics and offering the possibility of finding deviations from the Standard Model, forbidden decay processes or production of new particles with an unprecedented sensitivity [7].

Within its lifetime of about 15 years, four major operation modes with their respective energy levels are projected.

The first step is a centre-of-mass energy of 91.2 GeV to reach out for the pole mass of the Z boson. There, a electroweak-coupled new physics could be found. At the next step of 162.5 GeV the mass of the W boson could be measured with precision of a few tenths of MeV. At the intermediate step at 240 GeV, which would take place approximately 6 years after the first launch of the FCC-ee, the Higgs boson - as the least understood of all particles - and its couplings would be further investigated. The precision of the FCC-ee for those Higgs couplings would outstrip the precision of the currently upgraded High Luminosity Large Hadron Collider (HL-LHC) by an order of magnitude and is therefore capable of testing the quantum nature of the Higgs boson. In the last stage at 342.5 GeV the mass of the top quark is planned to be measured with precision of a few tens of MeV.

3.2 Collider Design

The accelerator is designed as a double ring synchrotron of an circumference of 97.756 km. It provides centre of mass energies from 88 to 365 GeV at two interaction points reaching luminosities from $3.1 \times 10^{34}\ \mathrm{cm}^{-2}\,\mathrm{s}^{-1}$ to $4.6 \times 10^{36}\ \mathrm{cm}^{-2}\,\mathrm{s}^{-1}$.

The layout of the collider is planned as part of the FCC integrated programs, which allows a later upgrade to an hadronic collider (FCC-hh) in the same infrastructure.

With an internal diameter of 5.5 m, the tunnel would be partly bored through the sedimentary rock in the Geneva Basin, passing under the lake Geneva, avoiding the limestone of the Jura, and partly mined through the Mandallaz limestone formation closing the loop through the molasses of the Arve valley [7]. The total length of about 100 km and in addition 8 km of bypass tunnels, 18 shafts, 12 large caverns and 12 new surface sites, makes the FCC one of the longest tunnels in the world, whose scope is comparable to the Gotthard Base Tunnel, which is the first flat low level route through the Alps ever built [8].

3.3 Synchrotron Radiation

As a key challenge and feature of circular e^+e^- accelerators, the synchrotron radiation power is limited to 50 MW per beam at all energies, which corresponds to a beam current of 1.4 A at a centre-of-mass energy of 45.6 GeV for the Z pole experiment and 5.4 mA at the top quark threshold at 182.5 GeV. The bending radius is planned to be 10760 m. Therefore for the Z pole experiment the main bending magnets are operated with a magnetic strength of 14.1 mT and with a magnet length of 23.94 m [7].

The proposed measurements of the transverse beam size uses the synchrotron radiation coming from the centre of the bending magnets. In the following, the shape of the radiation is examined with an analytic treatment.

Using approximations for relativistic energies and long magnets, the given magnet emits synchrotron radiation with the following amplitude function. It is given per electron per unit angle Ω depending on the frequency ω. Where ρ is the bending radius of the FCC, θ is the polar angle of observation, K is the modified Bessel function of second kind of given order, γ is the Lorentz factor, e is the elementary charge and c is the speed of light in vacuum. Most of the radiation is emitted over the polar angle θ, while the emission over azimuthal angle ϕ is reduced to the forward direction in this ultrarelativistic approximation [9].

$$\xi = \frac{\omega\rho}{3c}\left(\frac{1}{\gamma^2} + \theta^2\right)^{3/2} \tag{1}$$

$$A_{\parallel}(\omega,\theta) = \frac{e}{\pi\sqrt{3c}}\frac{\omega\rho}{c}\left(\frac{1}{\gamma^2} + \theta^2\right)\cdot K_{2/3}(\xi) \tag{2}$$

$$A_{\perp}(\omega,\theta) = \frac{e}{\pi\sqrt{3c}}\frac{\omega\rho}{c}\cdot\theta\cdot\sqrt{\frac{1}{\gamma^2} + \theta^2}\cdot K_{1/3}(\xi) \tag{3}$$

The $K_{2/3}$ represents the horizontal polarisation and $K_{1/3}$ the vertical. From those formulas one can deduct three essential statements to describe synchrotron radiation roughly.

The higher the energy, the narrower is the cone of light, the more energy is radiated in the horizontal polarisation plane and the higher are the frequencies that are radiated. This overall emitted intensity is depicted in Fig. 1.

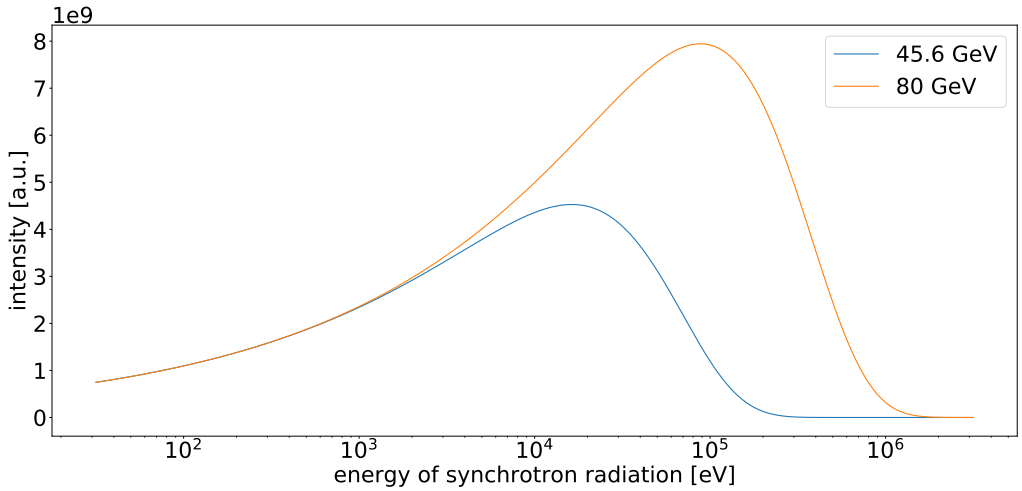

Figure 1: The radiation is integrated over all photon energies and all angles to obtain the total energy radiated from an FCC-ee bending magnet for the first two projected energies.

3.4 Transverse Beam Dynamics

One of the main goals of colliders is to achieve a high luminosity [10]. While letting the beams of the double ring synchrotron collide, their transverse profile is directly linked to the integrated luminosity, which is inherently essential to increase the statistical significance when looking for rare events like the decay of a Higgs boson. With the collision rate of the bunches f_{coll}, the number of particles in the bunches of the electron beam pipe n_1 and of the positron beam pipe n_2, and the transverse beam size σ_x in the horizontal and σ_y in the vertical plane, the integrated luminosity is [11]

$$\mathcal{L} = f_{coll} \frac{n_1 n_2}{4\pi\sigma_x\sigma_y} \tag{4}$$

The second main reason for observing the transverse beam size are the technical limitations of the accelerator. In order to protect the beam pipe and other sensible devices from scraping of the beam, apertures and collimators are installed throughout the ring. To keep the beam within those mechanical limitation, the beam size has to be monitored in order to be able to steer the beam with higher order magnets.

The boundaries of the relevant beam parameters that have to be dealt with are presented in the following table.

	Bunches	Charge (eV)	Current (mA)	Size in Arc (µm)
Min.	48	$1 \cdot 10^{10}$	0.005	H:60, V:10
Max.	16640	$2.3 \cdot 10^{11}$	1390	H:150, V:20

Table 1: The range of beam parameters which are of relevance for operation of beam diagnostic devices [7].

3.5 Transverse Beam Diagnostics

Measuring the transverse beam size involves several challenges. The accuracy has to be high enough to provide reliable data for the emittance monitoring and the method has to work fast enough to provide beam sizes on a bunch-by-bunch basis. For the LHC, there are different types of transverse beam size monitoring in use.

The Wire Scanner is the most basic and most referential technique. Its principles rely on the emission of secondary electrons from a thin carbon or tungsten wire, which is moved quickly through the beam. A given distribution of scattered electrons provides a basis for a reconstruction of the transverse beam size and as a consequence of the emittance. This method has its limitations due to the maximum energy which can be deposited on the wire. This is the reason why the Wire Scanner can not be used during a physics fill of the beam pipe, as the wire would break, and the beam would suffer too intense losses. It is more commonly used in the injector chain [12].

Secondary Emission Monitor (SEM) grids rely on the same principle as the wire scanner. The main difference is that they consist out of a fixed grid of wires and it is only used for single-pass locations (not on circulating beams) [13].

The Beam Synchrotron Radiation Telescope (BSRT) is a non-invasive synchrotron radiation imaging technique. One directly takes a picture of the synchrotron radiation source and by its width, the beam size can be calculated. Despite its advantage of being operational in all modes of the LHC, it is diffcult to do this kind of imaging with X-rays and its resolution is heavily affected by diffractional effects [10]

The Beam Synchrotron Radiation Interferometry (BSRI) uses visible light to perform interferometry at a double slit. The basic principle of this technique is similar to the one discussed in this thesis. Despite its success for visible synchrotron radiation it is difficult to extend the scheme to the range of X-rays because at those

wavelengths it is hard to fully block the radiation at the slit [14].

In the case of FCC-ee with extremely high electron beam and synchrotron radiation energies, the BSRT is no longer directly applicable as direct imaging in the X-ray domain is too difficult and diffractional effects become dominant. For the Wire Scanner, the beam itself would be too intense. A possible solution to overcome this limitations is the proposed technique of X-ray interferometry using near-field speckles, which adapts the BSRI for an X-ray range. Another possible profile measurement technique is the usage of a pinhole, although its resolution is quite limited.

4 Design and Theoretical Treatment

4.1 Idea and Description of the Measurement

The idea of the proposed technique is to measure the spatial coherence of the synchrotron radiation by interferometry and as linked via the Van Cittert Zernike theorem the transverse size of the beam. As shown in Fig. 2, synchrotron radiation is emitted from the core of the bending magnet. Then this photon beam is extracted from the beam pipe and filtered by monochromator to acquire a radiation of a certain bandwidth. This monochromatic beam is then scattered by a suspension of nanoparticles (hereinafter referred to as colloids). In a next step those scattered waves interfere with the transmitted waves, which are illustrated as plane waves. The interference of the many scattered waves with themselves is neglected as implied by the term heterodyne. Interference fringes only occur if there is coherence. This means that by the decay of the visibility of fringes one can calculated the area of coherence and thus the transverse size of the beam. The interference can only happen, if the scattered waves do not leave the area of the transmitted waves, which is the near field condition of this technique. This near field shall not be confused with the near field of an emitting dipole or of a dipole emitting synchrotron radiation.

The X-ray interference patterns are then visualised via a scintillator, converting the radiation to visible light. This image is magnified and projected onto a sensor over a mirror, which keeps the sensor and its electronics away from the X-ray path.

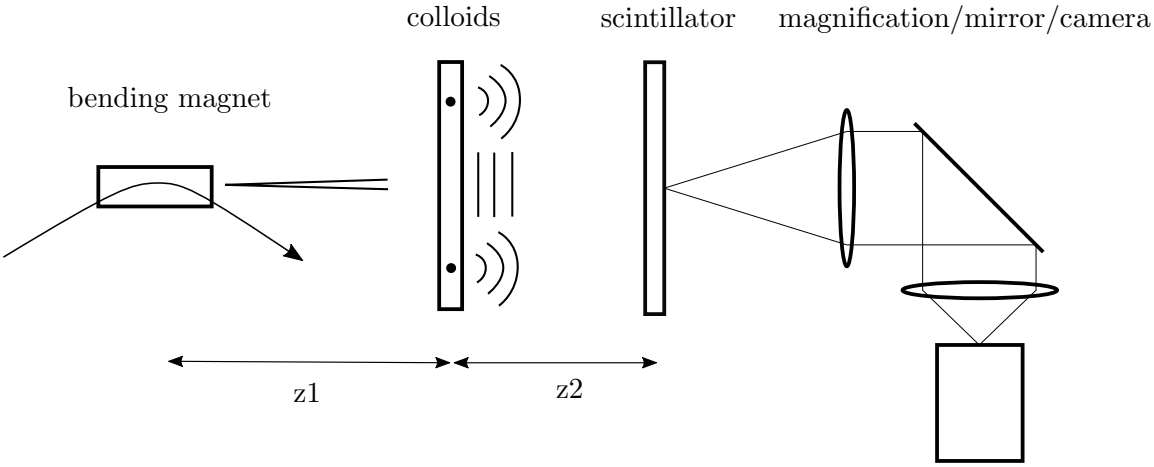

Figure 2: Schematic explanation of the proposed measurement

The interference of the diffraction of a few colloid is depicted in Fig. 3(a). Because the signal of this single scatterer would be too faint, a set of many randomly distributed colloids are used producing more and more of those identical interference patterns. At some point, the overlapping results in the typical speckles pattern

in Fig. 3(b) [15]. Even to the untrained eye, they will be recognisable as a more dotted and more granular structure compared to static noise. The actual decay of visibility of fringes is revealed in a 2D Fourier transformation in 3(c). Under perfect heterodyne conditions, the Fourier transformations of Fig. 3(a) and of Fig. 3(b) result in the same power spectrum as shown in 3(c).

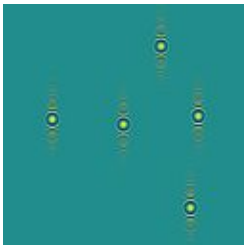

(a) Five randomly distributed colloids.

(b) A typical speckles [15] pattern of a few hundred randomly placed colloids.

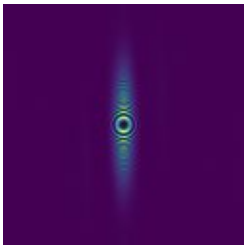

(c) The Fourier transformation of (b).

Figure 3: The three figures qualitatively illustrate the process of the measurement. In subfigure (a) the interference patterns of five randomly placed colloids are seen. The vertical elongation is a direct result of the beam size, which is much wider in the horizontal plane than in the vertical plane. Subfigure (b) is the actual speckle pattern which results by overlapping hundreds of the single colloids intereference patterns from subfigure (a). Subfigure (c) represents the Fourier transformation of subfigure (b). This power spectrum reveals the structure of the individual interference patterns.

The area of the coherence itself is visible through the decline of visibility of fringes of the power spectrum. This decay can be calculated or the horizontal and the vertical direction separately. As the colloids do not scatter uniformly in all directions, the decay of visibility of fringes is not only given by the decay of coherence but also due to their differential cross section which is also refered to as the scattering amplitude function [5].

4.2 Model of the Diffraction of the Radiation at Small Particles

Before the diffraction and the free-space propagation of the synchrotron radiation and all its predicted effects of coherence properties can be calculated easily, a model has to be found, which sufficiently precise maps the physical reality to a analytically manageable mathematical framework.

4.2.1 SRW

Synchrotron Radiation Workshop (SRW) was first published in 1997 [16]. It is an algorithm for numerical evaluation of synchrotron radiation for arbitrarily formed magnets including undulators in synchrotrons. The software is widely used and well proved in the field of studies on synchrotron radiation. It does not only calculate the electric field, but can also propagate this field through drift spaces, lenses, apertures or arbitrary 2D phase shifting and attenuating elements.

Its principles rely on numerically solving the Liennard-Wiechart potentials and propagating the wavefronts by numerically solving the Maxwell equations with help of Fourier Analysis [16] [17].

4.2.2 Model of the Radiation

The radiation that is generated as part of the acceleration of charged particles in the bending magnet is in its far field at the distance where the experiment is going to take place. It is commonly assumed, that the phase of the radiation behaves as if it was produced by a "point source", located in the middle of the bending magnet [18]. In the far field this spherical wave is then transferred into the form of plane waves. In reality the phase does not propagate resembling a spherical wave, but is much more complicated [19] [2].

Amplitude With help of SRW the amplitude of the synchrotron radiation at the FCC-ee is compared to the theoretical expression of the textbook reference (2) and (3) in Fig. 4. The measured amplitude fits well to the analytic expression from (2) and (3) in the central region. In the outer regions of the simulation the curves deviate up to 13 percent from the analytic prediction. This is interpreted to be not physical but rather a numerical error for the small values next to the boundary of the simulation's grid. A safety margin is therefore appropriate for all simulations with SRW.

[2] The deviation from a spherical wave is especially significant observing radiation coming from the edge of a magnet. For the given purpose, radiation coming from the centre of the dipole is going to be studied.

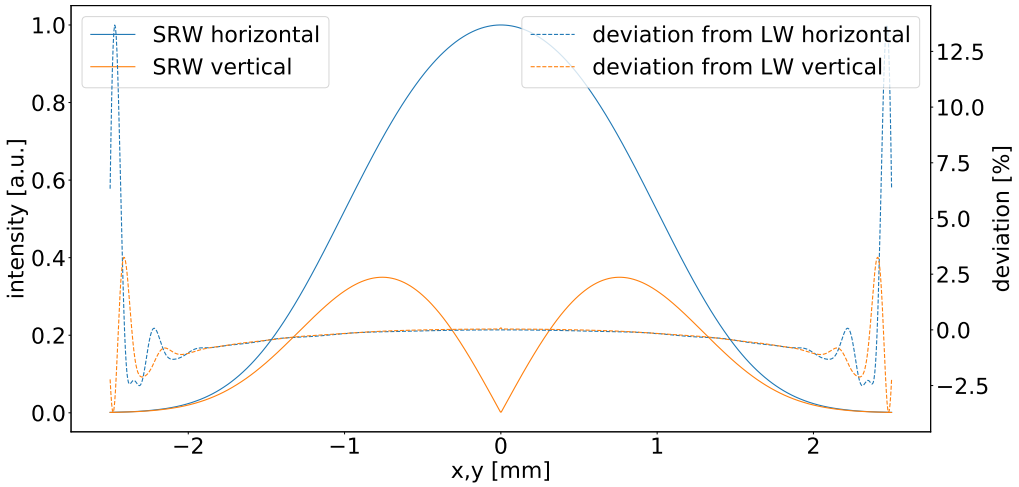

Figure 4: Comparison of the theoretical and the simulated amplitude of the synchrotron radiation at an FCC-ee bending dipole for a wavelength of $\lambda = 0.1$ nm. The left y-axis shows the intensity of the amplitude simulated by SRW and the right y-axis indicates the deviation from the theoretical formula in percent.

Phase Of much higher importance than the shape of the amplitude function is the deviation of the phase from the theoretical assumption which is depicted in Fig. 5. The difference between the spherical wave from an imaginary point source and the simulated phase ranges from -1 µrad to 4 µrad, whereas (similar to the amplitude) the central regions show less deviation than the outer regions.

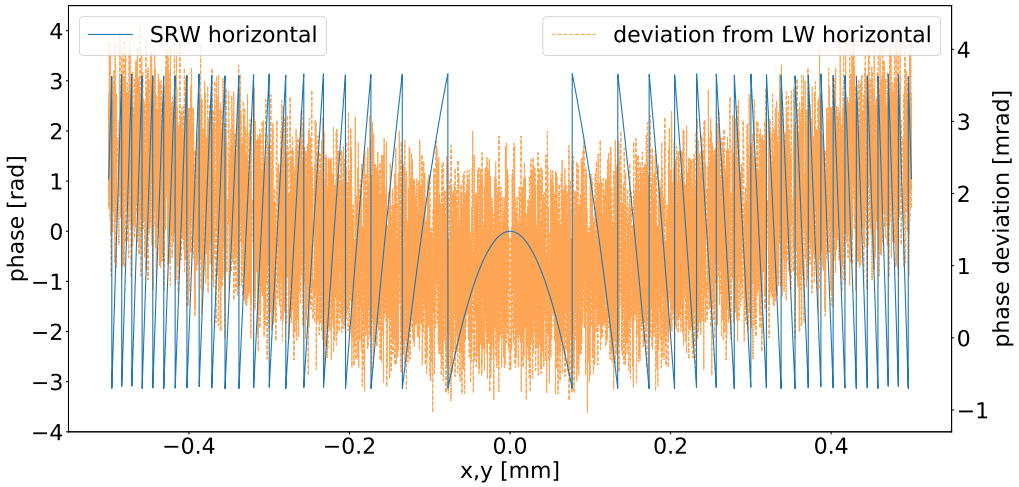

Figure 5: Comparison of the spherical approximated theoretical and the simulated phase of the synchrotron radiation at an FCC-ee bending dipole. The left y-axis shows the phase of the radiation simulated by SRW in radians and the right y-axis indicates the deviation from the phase of a spherical wave in micro radians.

The phase function corresponds to an sufficient extent to the assumption of a spherical wave. That means that the synchrotron radiation in the far field can be modelled using spherical waves, with an amplitude function shaped by the cited analytic evaluations of the Liennard-Wiechart potentials.

4.2.3 Excursus - A Short History of Diffraction

The many steps of exploring the nature of light since the 17th century is one of the most illustrative historical examples of the scientific method, its positivist believes and the interplay of hypothesises, theories and falsifications.

It started with Rene Decartes (1590-1650) being the first concerned with the intrinsic nature of light and the laws of optics. He compared the reflection of light with the bounce of balls and he published Willebrord Snellius's (1580-1626) law, first introducing certain factors for different materials. Snell's empirical law was then derived by Pierre de Fermat (1601-1675) by his principle of least time, providing an explanation to Snells ad hoc hypothesis. Sir Isaac Newton (1642-1727) was then the paragon - notably the first describing colour as an intrinsic quantity of light itself and not of the material - advocating the particle nature of light with his corpuscular theory even though not being able to explain diffractive phenomena. Newtons contemporary Christian Huygens (1626-1695) believed light to consist out of waves,

propagating through the ether like sound through air. He elucidated light as longitudinal waves of finite speed, limited by elastic decelerating collisions in the ether. In spite of his disbelief of the ether, he formulated a successful principle, modelling propagation as the interference of spherically radiating wavelets arising from the wavefront. He postulated, that those secondary wavelets are a direct result of the collisions in the ether. Despite this theory's success it was Newton's status that kept the corpuscular theory predominant until Thomas Young (1773-1829) performed his famous double-slit experiment, strengthening the positions of the followers of the wave theory and finally linking colour of light to its wavelength. Still a controversial and counterintuitive hypothesis it was Augustine Jean Fresnel (1788-1827) who convinced his contemporaries Pierre-Simon Laplace and Simon-Denis Poisson of the secondary wavelets by developing a natural explanation combining Huygens principle and Young's results. Finally James Clerk Maxwell (1831-1879) linked electric and optical phenomena with the electromagnetic theory and Gustav Kirchhoff (1824-1887) provided a rigorous mathematical formulation of Fresnels theory. A typical problem on the late 19th and early 20th century was the diffraction at spherical particles. It was Gustave Mie (1868-1957), giving a complete solution to this special case in 1908 [20] [21]. This complete solution is going to be used in the following.

4.2.4 Model of the Diffraction

As insinuated in the thesis's title, the diffraction of the monodispersed spherical nano- or microparticles in a suspension (hereinafter referred to as colloids) is studied in so-called near field heterodyne conditions.

The principle of the heterodyne condition is, that there is a strong transmitted and weak scattered beam. Only in that case the transmitted beam can serve as a local oscillator for the scattered beam and the homodyne terms - those are the interference terms between scattered waves themselves - can be neglected. Obeying this guideline, the percentage of the intensity of the scattered beam is set to 10% of the intensity of the transmitted beam.

The principle of the near field is not to be confused with the near and the far field approximation of the Fresnel–Kirchhoff diffraction formula. In the given case the term near field refers to that range behind a scattering object, where there scattered waves do not leave the area of the initial beam. Let us introduce a transverse beam size D, a wavelength of the observed synchrotron radiation λ, a radius of the colloids a and a point of observation at distance z behind the colloids. With those variables the near field describes the region [3]

$$z << a \cdot D/\lambda \tag{5}$$

This means, that only a region shall be considered where the transmitted beam still interferes with the scattered beam, because only the transmitted beam carries

information about the spatial coherence imposed by the finite size of the source. As soon as the scattered waves pass out of the path of the transmitted beam, it does not reveal information about the spatial coherence anymore. After this point one can still acquire information about the shape of the scattering particle but not about coherence properties of the initial beam.

An exact solution of the Maxwell equations for a plane wave passing through a spherical object of arbitrary size is the Mie theory [21]. This theory is going to be used to calculate the cross section of each colloid and as a consequence the total scattered intensity of the colloidal ensemble, which is necessary to find the optimal parameters for a heterodyne condition. This is done in the experimental section in 6.2.2. For the theoretical part the Mie theory is going to be used to calculate the amplitude scattering function, which is inherently essential to be able to find the spatial coherence of the synchrotron radiation. Finally properties of the phase behaviour are examined to find a good model for further simulations.

As mentioned, the decay of visibility of fringes is not only due to the actual decay of coherence but also due the differential scattering cross section $\mathrm{d}\sigma/\mathrm{d}\theta$, which is the absolute square of the scattering amplitude function or the scattered field amplitude $S(\theta)$.

$$\frac{\mathrm{d}\sigma}{\mathrm{d}\theta} = |S(\theta)|^2 \tag{6}$$

For our case, the radiation is in the region of hard X-ray, and the refractive index $n = 1 - \beta + i\delta$ of the colloidal material in this range is very small. To be more precise, the real part β of the refractive index, which accounts for refractive effects is small if compared to zero, and the imaginary part δ, which causes absorption and as a consequence diffractive effects is very small compared to zero and can be neglected. Additionally the wavelength of the radiation is small compared to the size of the colloids. For those range of parameters the results of the Mie theory can be approximated with the so called Anomalous Diffraction [20].

In the case of Anomalous Diffraction the function of the scattering amplitude function is

$$S(\theta) = i\rho k^2 a^2 \left(\frac{\pi}{2\zeta^3}\right)^{1/2} J_{3/2}(\zeta) \tag{7}$$

Where the refractive index is $n = 1 - \beta + i\delta$. Using $\rho = 2ka\delta$, $\zeta = ka\theta$, θ being the angle of the scattering, k the wavevector of the radiation and a the radius of the scattering particle. $J_{2/3}$ is the Bessel function of first kind of order $^2/_3$.

In order to proof the validity of this approximation for the given case, the scattered field amplitude of the Anomalous Diffraction is compared with the result of the more rigorous Mie Theory. A numerical algorithm for the evaluation of the Mie

Theory for spherical objects has been used [22].

The comparison has been made for synchrotron radiation of $E = 20$ keV, colloids with a radius of $a = 500$ nm and a refractive index of $n = 1 - 1.28 \cdot 10^{-6} + 2.49i \cdot 10^{-9}$. In addition to the rigorous Mie Theory of scattering and its approximation of the Anomalous Diffraction two other function are included for illustrative reasons and further studies.

The first one is a Gaussian fit of the Anomalous Diffraction, which is going to be useful for an analytic treatment in the Fourier domain. The second one is the diffraction pattern according to the Fraunhofer theory in the application of a circular aperture, also known as the Airy pattern. It would be applicable, if the particle and the wavelength were of comparable dimension and for a big refractive index. This pattern is going to be used later on, when the Optical Transfer Function is determined with help of visible light.

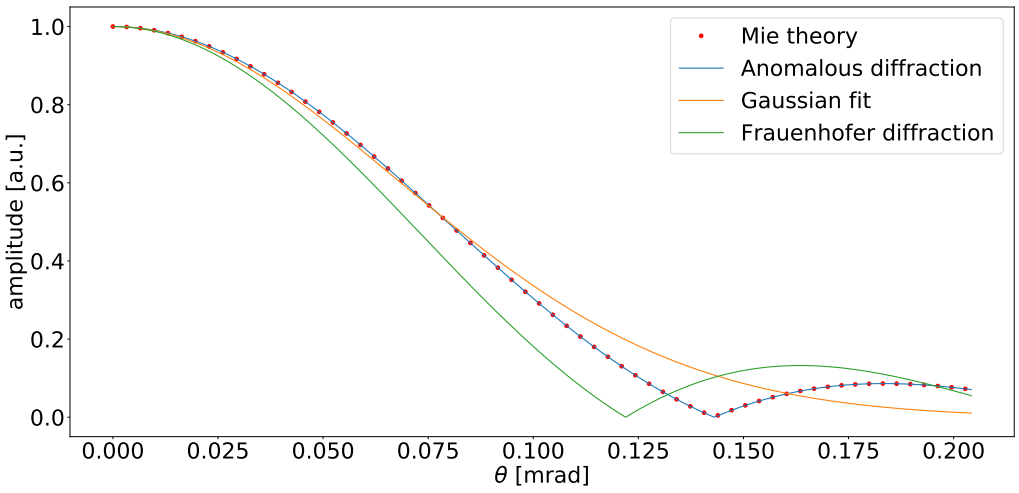

Figure 6: Comparison of the Mie theory and the Anomalous Diffraction for $n = 1 - 1.28 \cdot 10^{-6} + 2.49 \cdot 10^{-9}i$, and $\lambda = 6 \cdot 10^{-11}$ m in addition to a Gaussian fit of the Mie theory and the Frauenhofer diffraction for a big refractive index

The suggested approximation is therefore shown to be suitable for the given case. In coordinates of x the Gaussian fit of $S(\theta)$ with $\theta = \tan(x/z_2)$ has an approximated standard deviation of

$$\sigma_{scat} = 0.4793 \cdot \frac{\lambda z_2 \sqrt{2}}{2a} \tag{8}$$

Introducing the constant C_{scat}, the scattering amplitude function in dependence on

x and k is

$$S(k,x) = \exp\left(-x^2k^2\left(\frac{2a}{4\cdot\pi\cdot 0.4793\cdot z_2}\right)^2\right) = \exp\left(-x^2k^2C_{scat}\right) \tag{9}$$

Having found an appropriate function for the scattering amplitude, the next step is to examine the properties of the evolution of the phase downstream the colloid. For that CELES [23], a GPU accelerated MATLAB code is used, which is capable of evaluating the Mie theory for a large amount of colloidal particles and especially of the actual electric field.

In the dimensionless units of the code a colloid is set, which size is 100 times bigger than the wavelength of the incoming radiation. As for the calculation of the scattered field amplitude a refractive index of $n = 1 - 1.28\cdot 10^{-6} + 2.49i\cdot 10^{-9}$ is chosen.

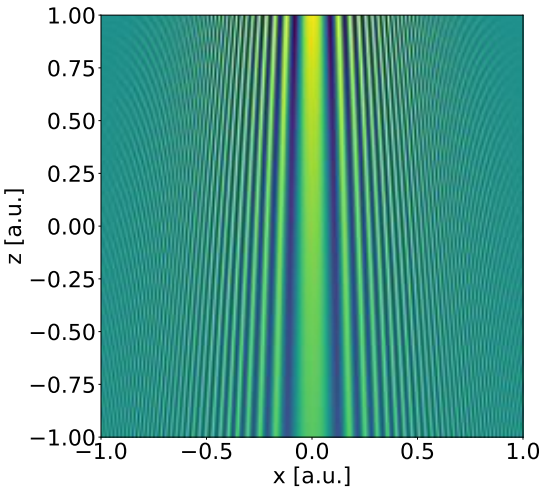

Figure 7: Lateral view of the refraction of an electromagnetic wave at a colloid, with a radius 100 times bigger than the wavelength of the incoming wave and with a refractive index of $n = 1 - 1.28\cdot 10^{-6} + 2.49i\cdot 10^{-9}$. The colours indicate the intensity of the electromagnetic field.

As to be seen in Fig. 7, due to the small refractive index there is almost no phase lag between the plane transmitted and the spherical excited wave, which means that there is positive interference in the centre of the speckle pattern. In addition to that, the interference follows the interference of a plane and a spherical wave.

To sum it up, an model was found, which is easy to manage and which is capable

of describing the scattering of a planar wave at a particle with sufficient accuracy. This model includes the following assumptions.

1. The colloid emits a spherical wave.
2. The spherical wave is shaped by the Anomalous Diffraction pattern which can be approximated by a Gaussian.
3. There is no phase lag between the exciting and the emitted wave, yielding a bright spot in the centre of the diffraction.

4.3 Decay of Visibility of the Scattered Radiation

4.3.1 General Theorems

Coherence describes the correlation between the electromagnetic fields sampled in two points and two time instants. Coherence is the property which enables light to create stationary interference patterns [24]. If there is no coherence the interference patterns are existent but not stationary.

In general the coherence is written in terms of the cross correlation function $\mathcal{R}_{i,j}$, which calculates the average in time of two points in the electromagnetic field E with indices i and j. The time average is denoted by angle brackets.

$$\mathcal{R}_{i,j} = \frac{1}{T}\int_0^T E(x_i, t_i + \tau) \cdot E(x_j, t_j + \tau)^* d\tau = \langle E(x_i, t_i) \cdot E(x_j, t_j)^* \rangle \tag{10}$$

The cross correlation function varies between a zero, indicating no correlation at all and a maximum, showing that those two points in space and time are in perfect agreement for all times.

In the following treatment, only one spatial dimension will be studied for the sake of simplicity. This can be done without loss of generality because of the dimensional linearity of coherence.

4.3.2 Temporal Coherence

The proposed idea of probing the coherence of synchrotron radiation with colloids is illustrated in Fig. 8. To start with, a single electron travelling through the beam pipe is modelled. This radiation is going to be spatially fully coherent, as a single electron can be treated as a point source. Temporally it is going to be only partially coherent, due to its finite bandwidth.

In a first step, radiation is emitted from an electron passing through the bending magnet in point s. After a distance z_1, the emitted synchrotron radiation hits a

colloid at point j. A small fraction of the radiation is scattered by this colloid and the scattered wave is going to expand spherically around the colloid as previously shown in the model of the diffraction. Nevertheless the transmitted wave passes on. It is drawn in straight lines, because provided that z_1 is much bigger than the transverse beam size, the transmitted wave is going to behave like a plane wave. After a distance z_2, an image will be formed capturing the interference of the transmitted and the scattered wave.

Let us focus on the intensity of the image at the point p. Here, at a certain point in time t one will measure the sum of the transmitted and the scattered wave, where the latter will be delayed by a time $\Delta t = t_i - t_j$. That means that by measuring the intensity of the electric field at point p, one actually probes the cross correlation between point i and j with a certain separation in time and space.

Using the total distance $z_3 = z_1 + z_2$ and the speed of light c as the propagation speed of the radiation, the time lag Δt is

$$c \cdot \Delta t(x) = z_1 + \sqrt{z_2^2 + x_p^2} - \sqrt{z_3^2 + x_p^2} \tag{11}$$

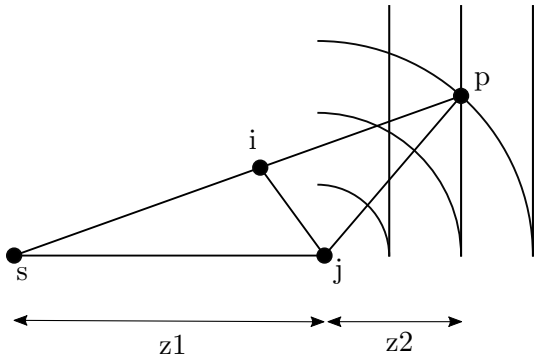

Figure 8: The interference of the scattered and the transmitted wave illustrates the measurement of the coherence between two points in the electromagnetic field.

This model of Fig. 8 can also be put in different but physically and mathematically equal perspective. In that view one neglects the scattered waves and writes the coherence in terms of an auto-correlation function of the transmitted wave with a weakened and time shifted copy of itself. In general, the auto-correlation calculates the correlation of a signal with the same signal shifted by a time Δt. This gives the following expression, where the correlation is integrated over a large time T.

$$\Gamma(x_p, \Delta t) = \frac{1}{T} \int_0^T E(x_p, \tau) \cdot E(x_p, \Delta t + \tau)^* d\tau = \langle E(x_p) \cdot E(x_p, \Delta t)^* \rangle \tag{12}$$

In the following the averaged intensity is introduced as $I(x) = \langle E(x) \cdot E(x)^* \rangle$ to define the normalised auto-correlation function.

$$\gamma(x,t) = \frac{\Gamma(x,t)}{\langle E(x) \cdot E(x)^* \rangle} = \frac{\Gamma(x,t)}{I(x)} \tag{13}$$

To illustrate the effect of the coherence for the given topic lets call the electric field of the transmitted wave E_1 and the one of the weakened time shifted wave E_2. E_2 will be attenuated by a factor I_{scat}.

$$E_2(x,0) = E_1(x,\Delta t) \cdot I_{scat} \tag{14}$$

They are now going to be superimposed, i.e. added at a general point x. The resulting intensity of the interference of those waves is given by the following formula, suppressing the temporal argument if it is zero [25].

$$\begin{aligned} I(x) &= \langle E(x) \cdot E(x)^* \rangle \\ &= \langle (E_1(x) + E_2(x)) \cdot (E_1(x) + E_2(x))^* \rangle \\ &= I_1(x) + I_2(x) + \sqrt{I_1(x) \cdot I_2(x)} \cdot \gamma_{1,2}(x,\Delta t) \end{aligned} \tag{15}$$

This result is based on the following symmetry

$$\Gamma(x,\Delta t) = \langle E_1(x,0) \cdot E_1(x,\Delta t)^* \rangle = \langle E_1(x,\Delta t) \cdot E_1(x,0)^* \rangle \tag{16}$$

It has been now shown in a general way how a certain time lag yields a stationary interference pattern. This is going to be applied for the given case of synchrotron radiation being scattered at nanoparticles.

The polychromatic beam is modelled as a sum of point like emitters at point s in the centre of the coordinates. Those point sources emit different frequencies with weights of their intensity G_j. The photon beam is going to be monochromated, but it will still remain polychromatic to some extent.

$$E(\vec{x}) = \sum_{j=1}^{N} \frac{\exp\left(ik_j|\vec{x}+\vec{z}| + ik_j ct\right))}{|\vec{x}+\vec{z}|} \cdot G_j^{\frac{1}{2}} \tag{17}$$

Inserting into the auto correlation function (12) gives

$$\Gamma(x,t) = \frac{1}{T}\int_0^T E(x,\tau) \cdot E(x,\Delta t + \tau)^* d\tau \tag{18}$$

In power square of the electric field everything gets cancelled out except the oscillation term of Δt. Letting the sum then converge to an integral and casting the different wavevectors on an arbitrary spectral density function $G(k)$, yields a closed form which resembles a Fourier Transformation

$$\Gamma(x,t) = \int_0^\infty G(k) e^{-ik\Delta t} dk \tag{19}$$

This result is commonly known as the Wiener Khinchin Theorem where the Fourier transformation connects the spectral density function with the function of temporal auto-correlation [26]. The temporal auto-correlation is a representation of temporal coherence.

Given a certain bandwidth Δk of a Gaussian profile, the coherence length l_c is

$$\Delta l_c = \frac{1}{\Delta k} \tag{20}$$

This is like the common results of an uncertainty between two Gaussian Fourier pairs.

For the specific evaluation of the temporal coherence, the spatial expression of the time lag (11) is used. First a taylor expansion around $x = 0$ is applied

$$c\Delta t(x) = z_1 + \sqrt{z_2^2 + x^2} - \sqrt{z_3^2 + x^2} = \frac{x^2}{2z_2} - \frac{x^2}{2z_3} + \mathcal{O}(x^4) \tag{21}$$

For the spectral density function $G(k)$ a Gaussian profile with standard deviation σ_k around a central wavevector k_0 is introduced. With that the temporal coherence is

$$\Gamma(\Delta t(x)) = \int_0^\infty \exp\left(\frac{-(k-k_0)^2}{2\sigma_k^2}\right) \exp\left(-ik\frac{x^2}{2} \cdot \left(\frac{1}{z_2} - \frac{1}{z_3}\right)\right) dk \tag{22}$$

The Fourier transform of a Gaussian is a Gaussian with inverted standard deviation. Evaluating yields

$$\Gamma(\Delta t(x)) = \exp\left(-\frac{x^4\sigma_k^2}{8}\left(\frac{1}{z_2} - \frac{1}{z_3}\right)^2\right) \tag{23}$$

As to be seen later, for the proposed experiment the approximation $z_2 \ll z_3$ holds true. It means, that the distance between the colloids and the scintillator is much smaller than the overall distance between the source of the radiation and the scintillator.

An intuitive explanation of the loss of coherence due to polychromaticity can be given by imagining differently fast oscillating interference patterns which all start with the same phase in the center of the coordinates. The sum of those different interference patterns causes the decay of the fringes.

To conclude, the temporal coherence is constrained by the finite bandwidth $\Delta k/k$ of the monochromator. Another constraint to the temporal coherence is the pulse duration of the radiation. The duration of the radiation pulse of one electron passing through a bending magnet is

$$\Delta\tau = \frac{L}{v}\sqrt{1 - \frac{v}{c}} \tag{24}$$

whereby v is the velocity of the particle, L is the length of the magnet and c is the speed of light. This relativistic results is much smaller than the intuitively expected duration of $\Delta\tau = L/v$. For a beam energy of 45.6 GeV and a magnetic length of L=23.94 m, the pulse is 0.5 ps. Any time lag bigger than this pulse duration will not produce any interference pattern. This is because only a electron moving through the bending magnet is coherent with itself and not with any other electrons later in time.

The leading constraint of temporal coherence is not going to be the pulse duration but the polychromaticity of the radiation itself.

4.3.3 Spatial Coherence

In the treatment of the last chapter the effect of single electron emitting a polychromatic beam was examined. This model lead to an expression of the Wiener Khinchin Theorem of the temporal coherence.

Now a monochromatic radiation coming from a extended source is modelled. This means that the radiation is fully coherent in the temporal domain but is going to be partially spatially coherent.

The emittance of the beam is designed to be $\epsilon_x = 1.46$ nm and $\epsilon_y = 2.9$ pm respectively. With the corresponding beta functions the beam size varies (according to the table 1 given in in the introduction) between 10 µm for a minimum in the vertical plane and 150 µm for a maximum in the horizontal plane.

To model the effects of a finite source on the spatial coherence, many point like emitters of spherical waves are put at points x_k resembling the distribution of particles in the transverse beam profile.

The electric field is then observed in a certain distance downstream z at a given point x in the plane perpendicular to the direction of propagation, receiving just one wavevector k and its corresponding angular frequency ω. Additionally a random initial phase ϕ_k is included. The amplitude function of the synchrotron radiation is neglected, as it is supposed to be flat enough in the interesting regions for all reasonable sets of parameters.

$$E\left(x,t\right) = \sum_k \frac{\exp\left(ik|\vec{x} - \vec{x_k} + \vec{z}| + i\omega t + \phi_k\right)\right)}{|\vec{x} - \vec{x_k} + \vec{z}|} \tag{25}$$

Inserting such fields in (10) leads to the cross correlation function between the positions x_1 and x_2.

$$\begin{aligned}\mathcal{R}(x_1,x_2) = \frac{1}{T}\int_0^\infty \sum_k \frac{\exp\left(ik|\vec{x_1}-\vec{x_k}+\vec{z}|+i\omega t+\phi_k\right)}{|\vec{x_1}-\vec{x_k}+\vec{z}|} \\ \cdot \sum_{x_j} \frac{\exp\left(ik|\vec{x_2}-\vec{x_k}+\vec{z}|+i\omega t+\phi_j\right)^*}{|\vec{x_2}-\vec{x_k}+\vec{z}|} dt\end{aligned} \tag{26}$$

Applying the time average, only for $k = j$ there will be a non zero contribution because different sources do not have any phase relation. For $k = j$ the coherence is going to be maximal, i.e. it is assumed as one.

$$\mathcal{R}(x_1,x_2) = \sum_k \frac{\exp\left(ik|\vec{x_1}-\vec{x_k}+\vec{z}|-ik|\vec{x_2}-\vec{x_k}+\vec{z}|\right)}{|\vec{x_1}-\vec{x_k}+\vec{z}|\cdot|\vec{x_2}-\vec{x_k}+\vec{z}|} \tag{27}$$

For a big number of particles the sum converges into an integral, where we use a density function $S(x)dx$ to model the density of particles at a position x_k.

$$\begin{aligned}\mathcal{R}(x_1,x_2) = \int_{-\infty}^{\infty} \frac{\exp\left(ik\left(\sqrt{(x_1-x)^2+z^2}-\sqrt{(x_2-x)^2+z^2}\right)\right)}{\sqrt{(x_1-x)^2+z^2}\cdot\sqrt{(x_2-x)^2+z^2}} \\ \cdot S(x)dx\end{aligned} \tag{28}$$

The Taylor expansion of the distance is

$$\sqrt{(x-x_k)^2+z^2} = z + \frac{(x_k-x)^2}{2z} + \mathcal{O}^4 \tag{29}$$

For the phase critical complex exponential function the second order is used. For the denominator the first order is sufficient.

$$\mathcal{R}(x_1,x_2) = \int_{-\infty}^{\infty} \frac{\exp\left(\frac{ik}{2z}\left(x_1^2-x_2^2+2x(x_2-x_1)\right)\right)}{z^2}\cdot S(x)dx \tag{30}$$

Modulo irrelevant prefactors and substituting $\xi = \frac{k(x_2-x_1)}{z}$ this yields

$$\mathcal{R}(x_1,x_2) \propto \int_{-\infty}^{\infty} \exp(ix\xi)\cdot S(x)dx \tag{31}$$

This result reminds of the result of the temporal coherence. There, the Fourier transformation of the spectral density leads to the temporal auto-correlation. In this case, the Fourier transformation of the spatial distribution with the oscillation

factor ξ represents the spatial auto-correlation function. It is commonly known as the Van Cittert Zernike Theorem [24].

Similar to the treatment of the temporal auto-correlation function where the time variable of one field was set to zero to define the time lag Δt, also here the distance in space is going to be denoted by $x_2 - x_1 = \Delta x$. This is done without loss of generality as while fixing a certain distance Δx, the coherence is constant for all possible values of x_1 and $x_2 = x_1 + \Delta x$.

For the density of the source $S(x)$, a Gaussian distribution with standard deviation σ_x for the horizontal plane, and σ_y for the vertical plane is introduced. In the following the notation for the horizontal plane is used, but the same applies for the vertical plane respectively.

$$\mathcal{R}(\Delta x) \propto \int_{-\infty}^{\infty} \exp(ix\xi) \cdot \exp\left(\frac{-x^2}{2\sigma_x}\right) dx \tag{32}$$

The Fourier transformation of a Gaussian is a Gaussian with flipped standard deviation.

$$\mathcal{R}(\Delta x) \propto \exp\left(\frac{-\Delta x^2}{2} \frac{k^2\sigma_x^2}{z^2}\right) \tag{33}$$

To conclude, the standard deviation $\sigma_{vcz,x}$ of the coherence in the horizontal plane - denoted by the initials of Van Cittert and Zernike - is

$$\sigma_{vcz,x} = \frac{z}{k\sigma_x} = \frac{\lambda z}{2\pi\sigma_x} \tag{34}$$

The same holds true for $\sigma_{vcz,y}$ for σ_y.

The assumptions and approximations made in this derivation are the following:

1. in the farfield, the synchrotron radiation behaves like spherical waves
2. there is no phase relation between the electrons, which emit synchrotron radiation
3. the effects of transverse or longitudinal movement during the passage of the particles through the magnet are not taken into account
4. $z_3 \gg \Delta x$, i.e. the distance between the source and the measurement of the coherence is much bigger than the coherence area itself

An intuitive explanation of the loss of coherence due to extended source can be given as follows. Shifted sources produce shifted interference patterns. The sum of those shifted interference patterns causes the decay of the fringes.

The applicability of the Van Cittert Zernike Theorem for the peculiarities of the FCC-ee arcdipole is still to be tested in a detailed simulation.

4.3.4 Model of the Interferometry with Colloids

As a single electron moves through the magnet, it produces a fully spatial coherent light. Many electrons next to each other give rise to a partially spatial coherent light. On the other hand, having just a single frequency would yield a fully temporal coherent beam. As we are going to see a polychromatic light, this results in a partially temporal coherent light.

Both cases have lead to convenient analytic expression in the previous chapters. Spatial coherence itself is expressed by the Van Cittert Zernike Theorem (33) and temporal coherence itself by the Wiener Khinchin Theorem (19). Now both cases and the scattering amplitude function shall be discussed in a combined model for the scattering at a colloid.

It is not a priori evident how the three types of decay interact in a combined model. Therefore all three effects shall be rigorously calculated in one model.

As seen in section 4.2.2, the radiation coming from the dipole can be approximately modelled with point like emitters of spherical waves. The electric field is now evaluated with help of a sum of particles at different positions x_j, with each a sum of different wavevectors k. The electric field is then examined in the distance $z = z_3$ at a transverse point x.

$$E_1(x) = \sum_j \sum_k \frac{\exp\left(ik\sqrt{(x-x_j)^2 + z_3^2}\right)}{\sqrt{(x-x_j)^2 + z_3^2}} \tag{35}$$

Those plane waves are now going to hit a single colloid at position $z = z_1$ and $x = 0$. The colloid picks up the phase of the incoming wave and scatters a spherical wave for each of the position and wavevectors of the initial radiation. Additionally the scattered wave is shaped by the scattering amplitude function $S(k, x)$.

One should note that the initial energy of the scattered wave is obviously too big. To be rigorous, one should scale the scattered wave according to the cross section of the colloid, but that is irrelevant for this model for now as we put our focus just on the shape of the interference term. The calculation of the total scattered energy is to be discussed in chapter 6.2.2.

$$E_2(x) = \sum_j \sum_k \frac{\exp\left(ik\sqrt{x^2+z_2^2} + ik\sqrt{x_j^2+z_1^2}\right)}{\sqrt{x^2+z_2^2}} S(k,x) \tag{36}$$

The initial radiation and its electric field E_1 and the scattered electric field E_2 are now going to be measured at a point x in the image plane at distance z_3. A few exceptions and assumption are made.

1. Only the field of the interfering term $E_1 \cdot E_2$ is observed. This interfering term is the eponymous heterodyne term. The terms $|E_1|^2$ and $|E_2|^2$ are the homodyne terms. This homodyne term of E_2 is commonly used to measure the size of the colloids [2].

2. As previously shown only waves of the same initial source particle and of the same energy are going to interfere. This is because different electrons are not coherent with each other.

3. The radial scaling of the waves power is neglected, because the focus is only on the shape of the heterodyne term.

Following those points the intensity of both interfering electric fields is

$$\begin{aligned} I(x) = |E_1(x) + E_2(x)|^2 \approx \\ E_1(x) \cdot E_2(x)^* + E_2(x) \cdot E_1(x)^* \propto \\ \sum_j \sum_k \exp\left(ik\left(\sqrt{(x-x_j)^2+z_3^2} - \sqrt{x^2+z_2^2} - \sqrt{x_j^2+z_1^2}\right)\right) S(k,x) + c.c. \end{aligned} \tag{37}$$

The complex conjugated term (*c.c.*) is going to be neglected for now and will be introduced again later on. Now the same series approximations as in (29) and the relation of the distances $z_3 = z_1 + z_2$ are used

$$\begin{aligned} \sum_j \sum_k \exp\left(ik\left[z_3 + \frac{(x-x_j)^2}{2z_3} - z_2 - \frac{x^2}{2z_2} - z_1 - \frac{x_j^2}{2z_1}\right]\right) S(k,x) = \\ \sum_j \sum_k \exp\left(ik\left[x^2\left(\frac{1}{2z_3} - \frac{1}{2z_2}\right) + x\left(-\frac{x_j}{z_3}\right) + x_j^2\left(\frac{1}{2z_3} - \frac{1}{z_1}\right)\right]\right) S(k,x) \end{aligned} \tag{38}$$

First, terms, which do not depend on x are neglected. Then the sums are replaced by integrals representing the distribution of source particles at positions x_j and the distribution of wavevectors k around a central k_0. Both are modelled by Gaussian functions with standard deviations σ_x and σ_k respectively. The expression of the

scattering amplitude function (9) is now inserted

$$\int_{-\infty}^{\infty} dk \int_{-\infty}^{\infty} dx_j \exp\left(\frac{-(k-k_0)^2}{2\sigma_k^2}\right) \exp\left(\frac{-x_j^2}{2\sigma_x^2}\right) \\ \exp\left(-x^2k^2C_{scat}\right) \exp\left(ik\frac{x^2}{2}\left(\frac{1}{z_3}-\frac{1}{z_2}\right)\right) \exp\left(-ik\frac{x\cdot x_j}{z_3}\right) \tag{39}$$

One can detect two Fourier transformations in custom frequency spaces. First the one over dx_j is performed yielding [3]

$$\int_{-\infty}^{\infty} dk \exp\left(\frac{-(k-k_0)^2}{2\sigma_k^2}\right) \exp\left(\frac{-k^2x^2\sigma_x^2}{2z_3^2}\right) \\ \exp\left(-x^2k^2C_{scat}\right) \exp\left(ik\frac{x^2}{2}\left(\frac{1}{z_3}-\frac{1}{z_2}\right)\right) \tag{41}$$

Here, the Van Cittert Zernike theorem becomes visible in the second exponential term. In the next steps, arguments of k are summarised to get a convenient quadratic form

$$\int_{-\infty}^{\infty} dk \exp\left(-k^2\underbrace{\left(\frac{1}{2\sigma_k^2}+\frac{x^2\sigma_x^2}{2z_3^2}+x^2C_{scat}\right)}_{\text{A}} + k\underbrace{\left(\frac{k_0}{\sigma_k^2}\right)}_{\text{B}} + \underbrace{\frac{k_0^2}{2\sigma_k^2}}_{\text{C}}\right) \\ \exp\left(ik\underbrace{\frac{x^2}{2}\left(\frac{1}{z_3}-\frac{1}{z_2}\right)}_{\xi}\right) \tag{42}$$

Again there is a Fourier transformation into the custom frequency space ξ. Evaluating gives

$$\exp\left(C+\left(\frac{(B+i\xi)^2}{4A}\right)\right)\frac{\sqrt{\pi}}{\sqrt{A}} \tag{43}$$

Now the complex conjugated which has been suppressed after (37) is introduced again and the terms are expanded while neglecting constant factors

$$\exp\left(\frac{(B+i\xi)^2}{4A}\right)+\left(\frac{(B-i\xi)^2}{4A}\right) = \\ \exp\left(\frac{B^2+\xi^2}{4A}\right)\cos\left(\frac{B\xi}{2A}\right) \tag{44}$$

[3] The Fourier transformation of a Gaussian with respect to a certain frequency ω is

$$\frac{1}{\sqrt{2\pi}}\int_{\infty}^{\infty}\exp\left(\frac{-x^2}{2a}+x\cdot b\right)\cdot\exp\left(-i\omega t\right)=\exp\left(\frac{(b+i\omega)^2a}{2}\right) \tag{40}$$

Rewriting the terms without abbreviations and with $C_{scat} \approx \lambda z_2/(2\sqrt{2}a)$ yields

$$I(x) = \exp\left(\frac{\frac{k_0^2}{\sigma_k^4} + \frac{x^4}{4}\left(\frac{1}{z_3} - \frac{1}{z_2}\right)^2}{\frac{2}{\sigma_k^2} + \frac{2x^2\sigma_x^2}{z_3^2} + 4x^2 C_{scat}}\right) \cos\left(\frac{\frac{x^2}{2}\left(\frac{1}{z_3} - \frac{1}{z_2}\right)\frac{k_0}{\sigma_k^2}}{\frac{1}{\sigma_k^2} + \frac{x^2\sigma_x^2}{z_3^2} + 2x^2 C_{scat}}\right) \tag{45}$$

In order to make reasonable approximations the orders of magnitude of the parameters are compared

1. $x = 0..10^{-3}$ m .. the observed grid is going to be in the range of millimetres
2. $\sigma_x = 10^{-7}$ m .. the beam size is a few tenths of µm
3. $k_0 \approx 6 \cdot 10^{-10}$ .. the synchrotron radiation energy is is going to be about 12.4 KeV
4. $\sigma_k \approx 10^6$ m^{-1} .. when using synchrotron radiation of 12.4 KeV with a bandwidth of 10^{-4}
5. $z_2 \ll z_3$ .. the distance between the colloids and the image plane z_2 will be a few meters and the distance between the emission at the dipole plane and the colloids will be around 100 m
6. $a = 10^{-6}$ m ..for colloids with a diameter of 1 µm

That justifies the following approximations

$$\cos\left(\frac{\frac{x^2}{2}\left(\frac{1}{z_3} - \frac{1}{z_2}\right)\frac{k_0}{\sigma_k^2}}{\frac{1}{\sigma_k^2} + \frac{x^2\sigma_x^2}{z_3^2} + 2x^2 C_{scat}}\right) \Rightarrow \cos\left(\frac{x^2 k_0}{2z_2}\right) \tag{46}$$

Let's introduce an abbreviation for the terms which are quadratic in x

$$C_{s,v} = \frac{2\sigma_x^2}{z_3^2} + 4x^2 C_{scat} \tag{47}$$

Applying a Taylor series around $x = 0$ for the both parts of the exponential function and using $z_2 \ll z_3$ yields

$$\exp\left(\frac{-x^4}{4x^2 z_2^2 C_{s,v} + 8z_2^2/\sigma_k^2}\right) = \exp\left(\frac{-x^4\sigma_k^2}{8z_2^2} + \mathcal{O}(x^6)\right) \tag{48}$$

$$\exp\left(\frac{k_0^2}{2\sigma_k^2 + \sigma_4 x^2 \cdot C_{s,v}}\right) = \exp\left(\frac{k_0^2}{2\sigma_k^2} - \frac{x^2 C_{s,v} k_0^2}{4} + \mathcal{O}(x^4)\right) \tag{49}$$

Summarising, skipping higher terms and constant prefactors and splitting $C_{v,s}$ leads to

$$I(x) = \underbrace{\cos\left(\frac{x^2 k_0}{2z_2}\right)}_{\text{fringes}} \cdot \underbrace{\exp\left(\frac{-x^4\sigma_k^2}{8z_2^2}\right)}_{\substack{\text{Wiener Khinchin} \\ \text{/temporal coherence}}} \cdot \underbrace{\exp\left(-x^2 k_0^2 \cdot C_{scat}\right)}_{\text{scattering}} \cdot \underbrace{\exp\left(-x^2 k_0^2 \cdot \frac{\sigma_x^2}{2z_3^2}\right)}_{\substack{\text{Van Cittert Zernike} \\ \text{/spatial coherence}}} \tag{50}$$

To sum up, an expression for the pattern produced by a single colloid for a polychromatic radiation of a finite source was found. It includes the fringes, the decay of the limited scattering and due to the spatial and temporal coherence.

The terms of the intensity are the product of the functions which were found in an individual treatment, which was somehow to be expected but not intuitively obvious. This holds true up to $\mathcal{O}(x^6)$ for the temporal coherence and it holds true up to $\mathcal{O}(x^4)$ for the spatial coherence and the decay to due to the amplitude scattering function.

In the previous calculations only one colloid has been considered. As written in the introduction, for many colloids there is interference between the scattered waves. To keep this interference negligible, the scattered intensity has to be weak in comparison to the strong transmitted beam.

4.3.5 Fourier Transformation of the Interference Pattern

If there was just one colloid, one could directly read the desired parameters from the measured intensity. As the signal of one single colloid is too faint to be measured, one has to use millions of colloids to have a significant signal. The scattered intensity is small, because of the small refractive index of the colloids material (silica) in the range of 10 keV to 20 keV radiation.

As a result of the use of many colloids, many shifted and overlapped pictures as in (50) give rise to the so-called speckle pattern or speckles [27]. This pattern differs from statistical noise by its granular structure, which is noticeable even to the untrained eye. In order to be able to acquire any information, one has to perform a two-dimensional Fourier transformation, which reveals the structure of a single interference pattern in the dual space.

In the following, the power spectrum of many randomly shifted intensity patterns is examined. The spatial frequency shall be called $q = {}^1\!/\!_x$. For the sake of convenience, for the upcoming Fourier analysis the oscillation term $-2\pi i$ without an normalisation factor is used, as this is equal to the algorithm of the Fast Fourier

Transformation in the numerical simulation later on.

$$I(q) = \left| \int_{-\infty}^{\infty} \exp(-2\pi i x q) \sum_{x_j} I(x - x_j) dx \right|^2 \tag{51}$$

In general the Fourier transform of a shifted function is

$$\mathcal{F} f(x - a)(q) = F(q) \exp(-2\pi i a q) \tag{52}$$

In the square of the absolute value the mixed terms of those random phases average out to zero, while the N homogeneous terms give rise to a signal.

$$I(q) = N^2 \cdot \left| \int_{-\infty}^{\infty} I(x) dx \right|^2 \tag{53}$$

Because of the higher order Gaussian of the temporal coherence, one cannot find an analytic expression for the Fourier Transformation. In practice there are two methods for a precise comparison of the measured signal and the theoretical approach. Either the measured pattern is going to be Fourier transformed and then reversely Fourier transformed, so that the measured intensity can be directly compared with (10). Or the Fourier transform of (50) is performed numerically and then compared with the power spectrum of the measured signal.

Nevertheless a rough estimation of the shape in the reciprocal space is going to be calculated in order to find an initial set of parameters. The Gaussian of higher order in (19), will be approximated by a Gaussian of standard order in (54), similar to the Gaussian fit of the Bessel functions for the amplitude scattering function (9). The approximation is done, so that the full width of half maximum is equal. This can be further improved later on with more precise approximations.

$$\exp\left(\frac{-x^4 \sigma_k^2}{8 z_2^2}\right) \approx \exp\left(\frac{-x^2 \sigma_k}{z_2} \sqrt{\frac{\log(2)}{8}}\right) \tag{54}$$

In the best possible experimental condition, the decay due to the spatial coherence is dominant over the decay due to temporal coherence or due to the limited scattering. In this ideal setup, the other terms of temporal coherence and limited scattering will only impose minor effects on the general decay of visibility of fringes.

Now the interference pattern can be summarised as

$$I(x) = \exp\left(-x^2 \underbrace{\frac{k_0^2 \sigma_x^2}{2 z_3^2}}_{C_1}\right) \cos\left(x^2 \underbrace{\frac{k_0}{2 z_2}}_{C_2}\right) \tag{55}$$

For now, C_1 only depends on the spatial coherence. As the temporal coherence and the scattering amplitude function can be expressed via Gaussians (see 54 and (9)), C_1 can be extended to also include those types of decay of visibility of fringes. This is because the product of Gaussian yields a Gaussian with the reciprocal sum of the inital standard deviation as a standard deviation.

Performing the Fourier transformation leads to

$$\mathcal{F}\left(\exp\left(-C_1x^2\right)\cos\left(C_2x^2\right)\right)(q) = \frac{\exp\left(\frac{-q^2\pi^2}{C_1-iC_2}\right)}{2\sqrt{2}\sqrt{C_1-iC_2}} + \frac{\exp\left(\frac{-q^2\pi^2}{C_1+iC_2}\right)}{2\sqrt{2}\sqrt{C_1+iC_2}} \tag{56}$$

For an estimation of the constants a central wavevector at 12.4 keV of $k_0 = 6 \cdot 10^{10}$ m^{-1}, a horizontal beam size of $\sigma_x = 10$ µm and a overall distance of $z_3 = 10^2$ m are used.

$$C_1 = \frac{1}{2}\left(\frac{6 \cdot 10^{10-5}}{10^2}\right)^2 \approx 2 \cdot 10^7 \text{ m}^{-2} \tag{57}$$

$$C_2 = \frac{\pi}{10^{-10+1}} \approx 3 \cdot 10^9 \text{ m}^{-2} \tag{58}$$

With $C_2 \gg C_1$ being used for the denominators the square of the absolute value is

$$I(q) \propto \exp\left(\frac{-2q^2\pi^2C_1}{C_1^2+C_2^2}\right)\sin^2\left(\frac{q^2\pi^2C_2}{C_1^2+C_2^2}+\frac{\pi}{4}\right) \tag{59}$$

where one sees an Gaussian envelope, and a squared sine of the squared spatial frequency, which are the so-called Talbot oscillations. Let us write the standard deviation of the spatial coherence from the Van Cittert Zernike Theorem as in (34)

$$\sigma_{vcz} = \frac{1}{2\sqrt{C_1}} = \frac{z_3}{k_0\sigma_x} \tag{60}$$

The standard deviation due to the partial spatial coherence, id est the Van Cittert Zernike theorem for the horizontal plane x in the q space is called $\sigma_{vcz,x,q}$. It is

$$\sigma_{vcz,x,q}^2 = \frac{1}{8\pi^2\sigma_{vcz,x}^2} + \frac{\sigma_{vcz,x}^2k_0^2}{8\pi^2z_2^2} \tag{61}$$

The result reveals a seemingly non intuitive anomaly. The first term inverts the width of the Gaussian as expected, but the second term is proportional to the initial shape, scaled by the frequency of the fringes. Because of $C_2 \gg C_1$ this second term is dominant for our case.

To put this more clearly, one can write not only the proportional scaling of the decay but also in general of the spatial variable in this regime.

$$q = x\frac{k_0}{\sqrt{2}\cdot 2\pi z_2} = x\frac{1}{\sqrt{2}\cdot\lambda z_2} \tag{62}$$

This result is generally known as the scaling in scattering. The additional factor $\sqrt{2}$ originates from the square of the absolute value of the Fourier transformation, which is necessary to get ride of the phase, which does not contain any essential information.

This scaling applies for the coordinates of the given area and therefore also for the different types of decays mentioned earlier. There is the decay of the temporal coherence with the Wiener Chinchin Theorem in the q space, called $\sigma_{wc,q}$ and there is the decay of the amplitude scattering function according to Mie and the approximation of the anomalous diffraction, called $\sigma_{mie,q}$.

$$\sigma_{vcz,q} = \frac{k_0}{\sqrt{2} \cdot 2\pi z_2} \cdot \frac{z_3}{k_0 \sigma_x} = \frac{z_3}{\sqrt{2} \cdot 2\pi \sigma_x z_2} \tag{63}$$

$$\sigma_{wc,q} = \frac{k_0}{\sqrt{2} \cdot 2\pi z_2} \cdot \sqrt{\frac{z_2}{\sigma_k} \sqrt{\frac{2}{\log(2)}}} \tag{64}$$

$$\sigma_{mie,q} = \frac{k_0}{\sqrt{2} \cdot 2\pi z_2} \cdot 0.4793 \cdot \frac{\lambda z_2 \sqrt{2}}{2a} = \frac{0.4793}{2a} \tag{65}$$

The last result is indeed remarkable, as there is no dependence on the distance or the wavelength but only on the size of the colloids.

Applying the approximation $C_2 \gg C_1$ also for the frequency of the sine term, the Talbot oscillations look like

$$T(q) = \sin^2\left(q^2 \pi \lambda z_2\right) \tag{66}$$

4.4 Instrumentational Setup and Optimisation

4.4.1 Separation of the Beam

Extracting synchrotron radiation from a synchrotron involves the challenge of separating the light from the beam such, so that the halo of the beam does not destroy the sensible extraction setup.

For the FCC-ee it is necessary to let both paths separate for at least 100 m until one can extract the light through a beryllium window [7]. At this position the distance between the light and the beam is approximately 10 cm.

4.4.2 Monochromator

For this experiment a well defined photon energy with a certain maximum bandwidth is necessary. For soft X-rays the usual way to create a customary bandpass filter are artificial periodical or natural gratings of crystal planes [28]. For hard X-rays the most commonly used technique are crystal monochromators [29].

In general for dealing with crystal monochromators, the wavelength of the photon energy, which shall be scattered, has to be comparable with the interplanar spacing d_{hkl} between the crystallographic planes. A crystal monochromator is based on the principles of refraction and therefore on Braggs's law.

$$\lambda = 2d_{hkl} \sin\theta \tag{67}$$

Here, θ is the angle of the beam's incidence on the crystallographic plane (hkl) and λ the wavelength of the scattered photon energy. The assumptions of Bragg's law are, that the crystal is perfect, that it has an infinite depth, and that the beam is perfectly collimated. Due to the finite size of the crystal and its imperfect and misaligned structure, and additionally because of the residual divergence of the beam, the monochromated radiation does not have an infinitely narrow bandwidth as suggested by Bragg's law. Other limiting effects are for example the mechanical strain being induced by the energy deposited within the material around the point of impact of the polychromatic beam. A higher thermal conductivity reduces this strain, as the material can be cooled more efficiently.

The most commonly used single crystal for monochromators is silicone. This is mainly due to the possibility of a large-scale industrial and cheap production of high quality silicon monocrystals. Another material used for these application is - albeit in smaller quantities - germanium. Its advantage is a higher conversion rate while on the contrary the thermal conductivity is lower than that of silicone [29].

There are several common designs to use single crystals as monochromators.

The double-crystal monochromator (DCM) consists out of two parallel aligned crystals. A chosen wavelength is reflected from the first crystals. As this first crystal receives the fully polychromatic beam, it has to be cooled. Then the beam impinges on the seconds crystal which directs the beam in its initial direction. For the second crystal, cooling is not necessary, because only a small fraction of the initial energy is reflected. This second part can be bent sagittally, if the beam has to be focused horizontally [29].

The channel-cut monochromator (CCM) is based on the same principle of having the beam reflected by two parallel crystal planes. Instead of aligning both

crystals, like for the DCM, a monolithic crystal is used in which a channel is milled along a crystallographic plane. This ensure that both planes are naturally aligned perfectly [29].

The imposed lateral shift of the beam allows to absorb the gamma ray photons being produced by the effect of the residual synchrotron radiation and the Beamsstrahlung. To achieve this, a tungsten block can be put after the first crystal.

A multilayer monochromator can be used for monochromatizing hard X-rays. Instead of using the natural crystal lattice, an artificial lattice is sputtered in thin layers. Usually there is a thinner sublayer of high-Z material and a thicker sublayer of low-Z material. The thickness of both layers on top of each other is Λ. This ensemble of two layers is repeated several times. Bragg's law for multilayers can be written as

$$\lambda = 2\frac{\Lambda}{m}\sin\theta \tag{68}$$

whereby the integer m = 1, 2, ... is the order of the reflection maximum [29].

The relative spectral width $\Delta E/E = \Delta k/k$ is to good accuracy a constant for a given Bragg reflection, and is in the range of $10^{-4} - 10^{-5}$ for low-indexed Bragg reflections, and can be as small as $10^{-9} - 10^{-10}$ for high-indexed Bragg reflections [30].

As an illustrative example the following design of the extraction setup is proposed.

1. As the synchrotron radiation is separated far enough from the electron beam, it exits the beam pipe through a beryllium window. Beryllium is very transparent to X-rays and therefore suitable for this task.

2. An aperture is put after the window, to select a rectangle of synchrotron radiation.

3. The lattice parameter of silicone with the Miller indices (111) is $d_{111} = 3.325$ Å [31]. Wavelengths of $\lambda = 1$ Å are therefore deflected at $\theta = 8.6°$. A second parallel silicon crystal is installed to guide the beam back to the horizontal plane. The separation shall be wide enough to be able to put a beam stop block around the first crystal.

4.4.3 Scattered Intensity and Behaviour of Colloidal Particles

Scattered Intensity The amount of light, which is scattered by colloids depends on the refractive index of the used material and the wavelength of the incoming radiation. Both those factors contribute to the extinction cross section $C_{ext} = C_s + C_a$, which describe how much light is either absorbed via the absorption cross section C_a or somehow redirected via the scattering cross section C_s [20]. The

real part of the refractive index (δ) is responsible for the refraction (C_s), and an imaginary part (β) accounts for diffractive effects (C_a). The full refractive index can be written as

$$n = \delta - i\beta \tag{69}$$

Given an initial energy of the radiation I_0, a extinction coefficient C_{ext}, the density of the colloids n and a depth of the suspension of colloids z, which the light has to pass, the actual scattered energy follows the exponential Beer-Lambert Law

$$\frac{I(z)}{I_0} = \exp\left(-z \cdot n \cdot C_{ext}\right) \tag{70}$$

The extinction cross section C_{ext} can be calculated via the extinction coefficient Q_{ext}, which is the ratio of the extinction cross section and the geometrical cross section. The size ratio between the colloid and the wavelength is $x = 2\pi a/\lambda$ and the phase lag through the colloid is $\rho = 2x(n-1)$ [20]. For optically soft materials and big values of the size ratio x, which is going to be the case for the proposed measurement, the Anomalous Diffraction Approximation of the Mie theory applies. Within this approximation there is an analytic form of the extinction coefficient in equation (71) [20].

$$Q_{ext} = \frac{C_{ext}}{\pi a^2} = 2 - \frac{4}{\rho}\sin\rho + \frac{2}{\rho^2} \cdot (1 - \cos\rho) \tag{71}$$

To find the right material for the colloidal scattering particles one has to take several things into account. As the particles are going to be suspended in distilled water, their density should not be much bigger than the one of the water. If they are too heavy, the would sediment too fast. On the other hand it is a fact that for a material with a higher atomic number Z and as a probable implication a higher density, the refractive index will be higher, especially for higher photon energies.

In Fig. 9 the absorption of light in silica microparticles with radius $a = 1$ µm is plotted, a promising candidates for the actual experiment. Another candidate would be gold, which has the advantage of a higher scattered intensity but with the disadvantage of a faster sedimentation. On the second y-axis the data is compared to the radiated power of the synchrotron radiation.

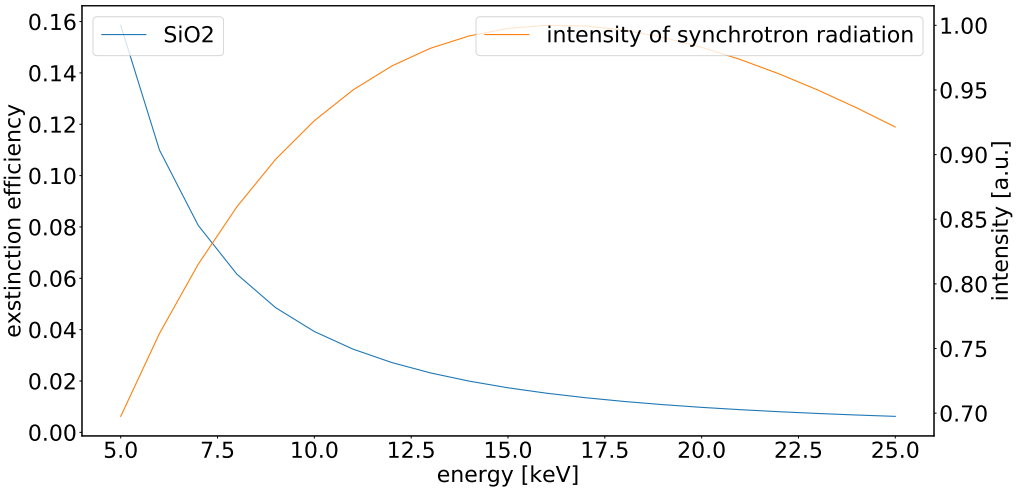

Figure 9: Absorption coefficient of silica is plotted in blue on the left y-axis and the power of the synchrotron radiation in sagittal direction is plotted in orange on the right y-axis.

Colloidal motion To compute the velocity of sedimentation Stokes law is used. The density of the suspension is ρ_w and the density of the colloidal particles is ρ_c. a is the radius of the colloids. The dynamic viscosity of the suspension is μ. The gravitational acceleration on earth is g. In general, the maximum velocity of falling sphere in a fluid is

$$v_{max} = \frac{2}{9} \cdot \frac{\rho_c - \rho_w}{\mu} g a^2 \tag{72}$$

The velocity depends directly on the density of the colloids. The densities are $\rho_w \approx 1$ g/cm^3 and $\rho_{silica} \approx 2.5$ g/cm^3.

The motion due to sedimentation has to be small in the time frame of the sensors exposure. The distance the particle moves within this exposure time has to be small compared to the resolution of the setup. Using the dynamic viscosity of water $\mu = 8.9 \cdot 10^{-4}$ kgm^{-1}s^{-1} and as an example a colloid radius of $a = 1$ µm the maximal sedimentation velocity of silica spheres is

$$v_{SiO2} = 3.7 \text{ µm} \tag{73}$$

To provide a reasonable resolution - of for example half a µm - the exposure time has to be shorter than 135 ms.

Since all materials sediment sooner or later, a regular shaking or rotating of the sample has to be ensured in any case. The advantage of a slower sinking of the particles is as shown, that the scattered image can be exposed longer without moving

particles causing artifacts in the Fourier space.

The Brownian motion of the particles in the fluid guarantees that the essential information of the interference pattern refreshes itself continuously. That means, that one can take a few images and by summing them up, the statistically fluctuating speckles average out and what is left is a static noise. Afterwards this static background can be subtracted from every of the following images. Having performed this subtraction of the static noise, only the relevant speckles are left. The advantage of this techniques is, that one can get ride of noise easily. On the other hand having particles in motion reduces the maximum possible exposure time.

If the static background noise is not a big problem, it would be a possibility to hold the particles in a gel or similar. This would allow an arbitrarily long exposure time, even if on has to forgo the self-renewal of the sample and its advantages. Another way of static scattering particles is to have material with microholes. According to Babinet's principle the diffraction pattern of an obstacle (the opaque colloidal particles within a transparent fluid) is identical to the one of apertures (the microholes in an opaque material).

In general, a solid material is preferable, as it is much more reliable for being put for a long time in the tunnel of a synchrotron. There is no need to worry about clumping or sedimentation of the particles. Studies are currently being carried out on this topic.

4.4.4 MTF of the Scintillator and the Optics

Working with high-energy X-rays in the range of tens of keV demands various requirements of the scintillation device [32].

First of all, there has to be a sufficient light conversion, to meet the requirements of the sensors sensitivity. Among other things, this depends on the X-ray stopping power which is based on the density and effective atom number of the material. Then, since the colloids are in continuous Brownian motion, there must be a corresponding time resolution. That means, that the so-called light remanence or after-glow has to be acceptably short. In addition, the device must withstand X-ray radiation to ensure good resolution over a long period of time. To conclude, non-toxic, easy machinable and commercially available materials are to be preferred.

For the present application, one of the most common scintillator on synchrotron sources is going to be used. It is a Ce-doped YAG single crystal scintillator on an inactive YAG substrate [33] with the following specifications listed in table 2

Chemical formula	$Y_3Al_5O_{12}$
Crystal structure	cubic
Density	4.55 g/cm^3
Emission maximum	550 nm
Conversion efficiency	4%
Refractive index	1.95
After-glow after 6 ms	<1%
Ce-doped YAG thickness	5-200 µm

Table 2: Physical and scintillating properties of the YAG:Ce [33]

The spatial resolution of a scintillator with finite thickness can be modelled as a defocused optical system, because images of the speckles pattern are produced at different positions throughout the depth of the scintillator.

In the following analytic approach by H.H.Hopkins [34] to calculate the frequency response $D(s)$ and by implication the modulation transfer function of this defocused system, a circular aperture is assumed and all scattering effects in the scintillator are neglected.

The optical transfer function is discussed in detail in chapter 6, while the following discussion rather focuses on the effects of the scintillator than on details of the spatial resolution of the optical system.

The distance from the focus point is called ζ, the numerical aperture NA and n the refractive index of the material. Additionally the longitudinal optical shift is defined as

$$\omega_{20} = \frac{\mathrm{NA}^2 \zeta}{2n} \tag{74}$$

Furthermore the frequency variable s

$$s = \frac{\lambda q}{\mathrm{NA}} \tag{75}$$

the factor a

$$a = \frac{4\pi\omega_{20}|s|}{\lambda} \tag{76}$$

and the upper angle β for the integration are introduced.

$$\beta = \arccos\left(\frac{|s|}{2}\right) \tag{77}$$

The frequency response for a certain defocused point ζ is

$$D(s) = \frac{4}{\pi a}\cos\left(\frac{a|s|}{2}\right)\int_0^{\beta}\sin\left(\cos a\,(\theta)\right)\cdot\cos\left(\theta\right)d\theta - \frac{4}{\pi a}\sin\left(\frac{a|s|}{2}\right)\int_0^{\beta}\cos\left(\cos a\,(\theta)\right)\cdot\cos\left(\theta\right)d\theta \tag{78}$$

Those integrals can be written in terms of a convergent series of Bessel functions, which are suitable for a numeric calculation.

$$D(s) = \frac{4}{\pi a}\cos\left(\frac{a|s|}{2}\right)\left(\beta J_1(a)\sum_{k=1}^{\infty}(-1)^{k+1}\frac{\sin\left(2k\beta\right)}{2k}\left[J_{2k-1}(a) - J_{2k+1}(a)\right]\right) - \frac{4}{\pi a}\sin\left(\frac{a|s|}{2}\right)\left(\sum_{k=0}^{\infty}(-1)^{k}\frac{\sin\left((2k+1)\beta\right)}{2k+1}\left[J_{2k}(a) - J_{2k+2}(a)\right]\right) \tag{79}$$

If one lets ω_{20} in (79) converge to zero, that means that everything is put into focus, the result is the same as (110), which is going to be used in chapter 6.

For the full optical transfer the results has to be integrated over all the range δz, which is out of focus, assuming that in the experiment, the focus is put in the center of the scintillator.

$$\mathcal{OTF}(q) = \int_{-\frac{\delta z}{2}}^{\frac{\delta z}{2}} D(q,\zeta)d\zeta \tag{80}$$

The modulation transfer function is the absolute value of the optical transfer function. As we do not put our focus on a possible phase shift, this is the essential function.

$$\mathcal{MTF}(q) = |\mathcal{OTF}(q)| \tag{81}$$

This is now evaluated for a numerical aperture of NA $= 0.4$ for the mentioned YAG:Ce with different thicknesses of $\delta z = 30..100$ µm in Fig. 10.

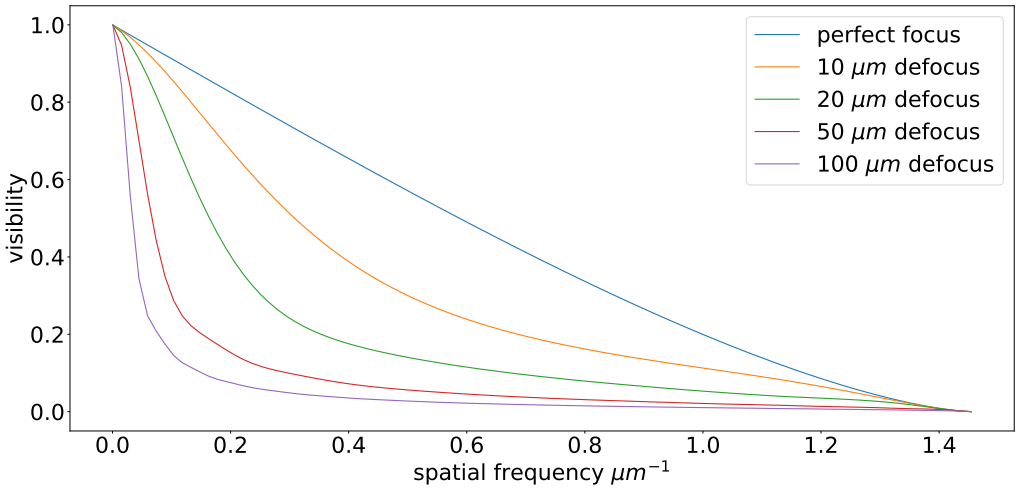

Figure 10: The figure shows the Modulation Transfer Function of a defocused system for different thicknesses of a YAG:Ce scintillator compared to a perfectly focused system.

Despite the advantage of a better modulation transfer function for thinner scintillators, the downside is the lower overall conversion efficiency. The absorption of X-rays and as a further consequence the emission of visible light proportionally follows the Beer Lambert law.

From those curves in Fig. 10, one can deduct that thinner scintillators are generally better in terms of resolution. The only limitation of reducing the thickness is the lower amount of light yield [4], which is needed to put enough light on the sensor within a certain exposure time. The challenge of the light yield is to be discussed in the next section.

4.4.5 Light Yield

In this section the intensity of the synchrotron radiation and its attenuation is roughly estimated in order to see what exposure time of the camera is appropriate for which setup of monochromator, colloidal particles and scintillator.
Considering the intensity of the synchrotron radiation, there are several challenges, which are to be dealt with. In the order of the beam line, the first issue is the power of radiation impinging on the monochromating crystal. Let us have a look at the energy which has to be dissipated.

[4] Despite the downside of having a weaker light conversion, a minimal thickness should be taken into consideration concerning a certain stability especially if cooling is necessary.

For the Z pole experiment with a beam energy of 45.6 GeV the maximum charge of the FCC-ee program of about 1.139 A is reached. Integrating the analytic formulas (2) and (3) over all frequencies yields a intensity distribution for each angle [9]

$$I(\theta) = \frac{1}{4\pi\epsilon_0} \cdot \frac{7e^2}{16\rho} \cdot \left(\frac{1}{\gamma^{-2} + \theta^2}\right)^{5/2} \cdot \left(1 + \frac{5}{7}\frac{\theta^2}{\gamma^{-2} + \theta^2}\right) \tag{82}$$

The cone of the synchrotron radiation, which is going to be used is going to span over approximately 10 µrad. If one selects this as the operational area in distance of $z_1 = 100$ m, where the radiation is separated sufficiently, a rectangular aperture of a size of 1 mm x 1 mm is appropriate to select this cone and to get rid of any other type of synchrotron radiation like Beamsstrahlung and to protect the devices (like the cooling setup of the monochromator) afterwards. At a beam energy of 45.6 GeV the energy drops to about 70% towards the edge of this cone. The horizontal size of the spot of the synchrotron radiation does not depend on radiation properties, as it is continuous in the range of the bending magnet because of the sweeping through of the beam. Integrating over this area of 1 mm^{-2} for a single electron for all photons energies yields a total power dissipation on the single crystal of $4.7 \cdot 10^{-13}$ W.

For the Z pole experiment with 45.6 GeV, the revolving time of a particle is 0.32 ms. With 16640 bunches with an electron population of $1.7 \cdot 10^{11}$ each, there are $2.82 \cdot 10^{15}$ electrons in total. It follows that $8.84 \cdot 10^{18}$ electrons pass through one beam pipe of the synchrotron each second. The synchrotron's circumference is 97765 m, whereas the overall length of the 2900 dipoles with a bending radius of 10760 m and a magnetic length of 23.94 m accounts for 71% of the circumference.

The design report states, that the synchrotron radiation per beam is limited to 50 MW at all stages. Another big part of this power is radiated via beamstrahlung, which is the radiation being emitted due two both charged beams and their strong electromagnetic fields passing close to each other in opposite directions.

Let us for the sake of simplicity ignore the structure of the bunching and consider a floating beam to get an average value. To calculate the energy deposited within the aperture on average, one has to consider that the total horizontal opening angle $2\theta = 10$ µrad, which sweeps over the aperture is approximately the same as the fraction of the imaginary cropped synchrotron - without any straight sections - which accounts for the particles emitting synchrotron radiation through this aperture. Furthermore one has to multiply by the length of all dipole length and divide by the total circumference to get an average value of the floating beam and its radiation. It follows that the opening of the 1mm x 1mm aperture receives an average of

$$P_1 = 4.7 \cdot 10^{-13} \text{ W} \cdot 8.84 \cdot 10^{18} \cdot \frac{10 \cdot 10^{-6}}{2\pi} \cdot 0.71 = 4.7 \text{ W} \tag{83}$$

As this is the energy on a square millimetre, it corresponds to a total irradiance of $E_1 = 4.7\ \mathrm{MW/m^2}$. This is the energy the material of the monochromator and its cooling system has to deal with.

The monochromator is going to pick a certain frequency with a certain bandwidth. The integration shall now be revisited for a photon energy of $E_\gamma = 12.4$ keV and a bandwidth of $\Delta E/E = 10^{-4}$.

Combining the field amplitude of (2) and (3), the energy radiated per unit frequency per unit angle per electron is [9]

$$\frac{dI(\omega)}{d\Omega} = \frac{1}{4\pi\epsilon_0} \cdot \frac{e^2}{3\pi^2 c} \left(\frac{\omega\rho}{c}\right)^2 \left(\frac{1}{\gamma^2} + \theta^2\right)^2 \left[K^2_{2/3}(\xi) + \frac{\theta^2}{\gamma^{-2} + \theta^2} K^2_{1/3}(\xi)\right] \tag{84}$$

A numerical integration with help of Riemann sum has been applied to sum over the area of the given cone of light and of the energy bandwidth. The same logic of the floating beam in a cropped synchrotron with a certain revolution of the population of electron gives a radiated power for the chosen energy and cone of light of

$$P_2 = 1.24 \cdot 10^{-17}\ \mathrm{W} \cdot 8.84 \cdot 10^{18} \cdot \frac{10 \cdot 10^{-6}}{2\pi} \cdot 0.71 = 0.13\ \mathrm{mW} \tag{85}$$

This is equal to an irradiance of $E_2 = 0.13\ \mathrm{kW/m^2}$ which is for a intuitive comparison about three times the solar constant.

Having performed the monochromating, the beam has to be scattered by the colloidal particles. The principle of the Heterodyne Near Field Speckles relies on a strong transmitted and a weak scattered beam, with about 10% of the initial energy. The number of the colloids has to be scaled in order to adapt to this fraction. As the refractive index, and as a consequence the absorption of the colloids decreases with higher photon energies, more colloids have to be used when dealing with smaller wavelengths. Because of this variable of the density of colloids, their refractive index has not to be considered in the ongoing analysis of the light yield. The next crucial step is the scintillator. Given the data from the scintillator supplier Crytur [35], the absorption of YAG:Ce for different thicknesses is plotted in Fig. 11.

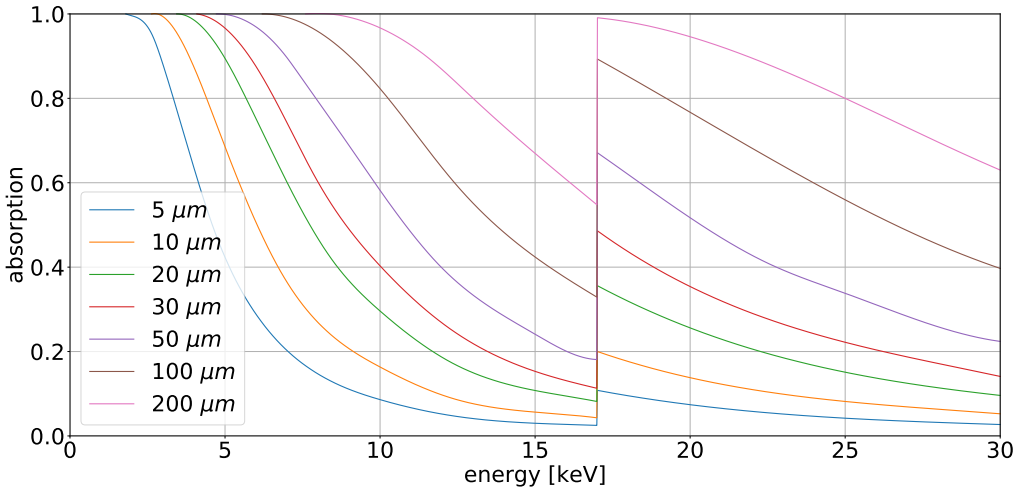

Figure 11: Absorption and conversion rates for different thicknesses of the YAG:Ce scintillator

The absorbed energy decreases with higher photon energies until an edge at a photon energy of $E_\gamma = 17$ keV. After the peak around this edge, the absorption decreases again. The photon yield per absorbed MeV for YAG:Ce is $\Gamma_\gamma = 3 \cdot 10^4 \gamma/\text{MeV}$ or $\Gamma_\gamma = 1.87 \cdot 10^{17} \gamma/\text{J}$ at a working wavelength of the scintillator of $\lambda_{scint} = 550$ nm [35]. For an example photon energy of $E_\gamma = 12.4$ keV the absorption for a $\delta z = 50$ µm scintillator is $\mu = 0.37$. That yields an absorbed intensity of 48 W/m^2 and an emitted photon flux of $\Phi = 8.58 \cdot 10^{18} \gamma/\text{s/m}^2$.

$$\Phi = E_2 \cdot \mu \cdot \Gamma_\gamma = 48 \frac{\text{J}}{\text{s m}^2} \cdot 0.37 \cdot 1.87 \cdot 10^{17} \frac{\gamma}{\text{J}} = 8.58 \cdot 10^{18} \frac{\gamma}{\text{s m}^2} \tag{86}$$

To analyse the photon flux on the sensor a typically CMOS camera is considered. The acA5472-5gm - Basler ace has a pixel size of $A_{px} = 2.4$ µm x 2.4 µm, a full well capacity (or saturation capacity) of $C = 13.8\text{k}e^-$ and a quantum efficiency of $QE = 75.2\%$ at $\lambda = 550$ nm. The photon flux, which is necessary to make the electron storage of the pixels full, id est to saturate the sensor to its maximum level within an exposure time of $t_{exp} = 5$ ms is

$$\Phi_{max} = \frac{C}{t_{exp} \cdot A \cdot QE} = 6.37 \cdot 10^{17} \frac{\gamma}{\text{s m}^2} \tag{87}$$

The results show that the source is too bright for the given setup by one order of magnitude. Even with an scintillator of $\delta z = 5$ µm, for which the absorption drops to $\mu = 4.7\%$ the photon count is still twice as high than necessary. Therefore light has to be attenuated in an early stage of the setup, to avoid unnecessary energy deposition or over-saturation in mission critical parts like the scintillator or the sensor.

To conclude, this rough estimation of the transferred intensity shows that a monochromator with $\Delta E/E = 10^{-4}$, a scintillator with a thickness $\delta z = 5$ µm and a exposure time of $t_{exp} = 5$ ms for a standard CMOS sensor are absolutely feasibly in terms of a sufficient light yield.

4.4.6 Optimising the Parameters

In the following a set of parameters shall be found, where the decay due to spatial coherence is leading in comparison to the decay due to temporal coherence and due to the scattering function. This dominant decay promises a precise measurement of the transverse profile of the beam. In addition, the specifications of the camera sensor and the numerical aperture of the magnification setup must be good enough to resolve the Talbot oscillations from equation (50) in the power spectrum with sufficient precision.

The constraints and restrictions that follow these ideal conditions are now listed.

1. The size of the beam at the source is the first fixed constraint. The standard deviation in the horizontal planes varies between 60 µm $< \sigma_x <$ 150 µm and in the vertical in the range of 10 µm $< \sigma_y <$ 20 µm. To start with, mean values are assumed for a first optimisation.

$$\sigma_x = 105 \text{ µm}$$
$$\sigma_y = 15 \text{ µm}$$

2. The distance between the bending magnet and the extraction set up shall be big enough to separate the light properly.

$$z_1 > 100 \text{ m} \tag{88}$$

3. The distance between the colloids and the detector z_2 shall be not too big in order to fit the setup on a standard optical table in the tunnel of the beam pipe. On the other hand the distance has to be big in comparison to the thickness of the cuvette, which holds the colloids. Usually this cuvette has a diameter of a few millimetres.

$$1 \text{ cm} < z_2 < 5 \text{ m} \tag{89}$$

4. The area of the spatial coherence shall be smaller than the area of the diffracted light. That implies that

$$0.4793 \cdot \frac{\lambda z_2}{2a} \cdot \sqrt{2} > \frac{\lambda z_3}{2\pi\sigma_{x,y}} \tag{90}$$

5. The area of the spatial coherence shall be smaller than the area of the decay due to the temporal coherence. Here a first order Gaussian approximation is used for the second order Gaussian representation of the Wiener Chinchin Theorem for the scattering at colloidal particles.

$$\frac{\lambda z_3}{2\pi\sigma_x} < \sqrt{\frac{z_2}{\sigma_k}\sqrt{\frac{2}{\log(2)}}} \tag{91}$$

6. With increasing λ and z_2 the interference fringes are oscillating faster and faster. In order to make a descent resolution, there has to be a certain maximal pixel size. If one aims to see a fringe in a distance of s_1 times σ_{vcz} with at least s_2 pixels, the maximal pixel size is dictated by the following calculation.

   The minima of the fringes

$$\cos\left(\frac{x^2}{\lambda z_2}\right) \stackrel{!}{=} 0 \tag{92}$$

   are at positions

$$x_n = \sqrt{\lambda z_2 n} \tag{93}$$

   The last fringe, which has to be resolved is at position

$$x_{n_{max}} = s_1 \cdot \sigma_{vcz} \tag{94}$$

   At this position one sees the fringe with number

$$n_{max} = \frac{x_{n_{max}}^2}{\lambda z_2} \tag{95}$$

   It follow that the fringe has a width of

$$\Delta x = \sqrt{\lambda z_2 n_{max}} - \sqrt{\lambda z_2 (n_{max} - 1)} \tag{96}$$

   To conclude, to be able to resolve this fringe with at least s_2 pixels the pixel size px has to be

$$px < \frac{\Delta x}{s_2} \tag{97}$$

7. A similar logic applies to the Fourier space, where the Talbot oscillations have to be resolved properly. As a pixel size was found in the latter calculation for the fringes in the direct space, now a field of view is going to be calculated for the Talbot oscillations in the Fourier space. With increasing λ and z_2 the Talbot oscillations are getting faster and faster. If they are oscillating too fast, one can not resolve them anymore. If one wants to see a certain width of $s_1 \cdot \sigma_{coh}$ in the Fourier transformation on a camera with p pixels on one axis

and a field of view of f, the distance between two peaks of the fringes at this width of $s_1 \cdot \sigma_{coh}$ shall still be bigger than a few s_2 pixels in the frequency domain.

Solving

$$\sin\left(q^2 \pi \lambda z_2\right) \stackrel{!}{=} 0 \tag{98}$$

gives

$$q = \sqrt{\frac{n}{\lambda z_2}} \ldots n \in \mathbb{N} \tag{99}$$

The utmost frequency which shall be resolved is

$$q_{max} = s_1 \cdot \sigma_q = s \cdot \frac{\sigma_{vzc}}{\sqrt{2}\lambda z_2} \tag{100}$$

At this frequency one sees the n-th fringe

$$n_{max} = q_{max}^2 \lambda z_2 \tag{101}$$

Rounding n_{max} to the next integer the distance of fringes at this frequency is

$$\Delta q = \sqrt{\frac{n_{max}}{\lambda z_2}} - \sqrt{\frac{n_{max} - 1}{\lambda z_2}} \tag{102}$$

To conclude, to resolve a fringe at this distance in frequency with at least s_2 pixels the frequency resolution of the Discrete Fourier transformation has to yield to the following

$$\frac{\Delta q}{s_2} > \Delta q_{DFT} = \frac{1}{f} \tag{103}$$

With the pixel size and the field of view f also the minimum amount of pixels p is determined.

8. The power received on the cameras sensor dictates a certain exposure time which has to small enough in order not to see blurry speckles due to sedimentation. As there is enough power, also with a narrow monochromated beam and a thin scintillator there are no limitations from this side of view.

4.4.7 Proposing a Set of Parameters

Vertical Plane For a mean vertical beam size of $\sigma_y = 15$ µm the Talbot oscillations oscillate really fast. The general challenge is to find a reasonable set parameters where those oscillations can be resolved sufficiently. Both higher energies, that means smaller wavelengths λ and bigger distance z_2 help to slow down the fringes to make a better resolution.

First the distance between the source and the colloids is fixed at $z_1 = 100$ m. Then the distance between the colloids and the scintillator is fixed at the largest possible value of $z_2 = 5$ m. Hence those given constraints lead to a maximum colloid radius of $a < 1.5$ µm.

To get as much intensity as possible and to choose the highest feasible energy in terms of the monochromating, the diffraction at the colloids and the scintillator, a wavelength of $\lambda = 6 \cdot 10^{-11}$ m is chosen. For that the energy bandwidth has to be $\sigma_k/k < 1.8\%$.

If one aims to see at least one sigma of the decay due to spatial coherence with a resolution of at least 5 pixels for the last fringe, the field of view shall be $f = 0.44$ mm with $p = 935$. The above-mentioned validates the following set of parameters in table 3 to be ideal.

parameter	value
σ_y	15 µm
λ	$6 \cdot 10^{-11}$ m
z_1	100 m
z_2	5 m
a	< 1.5 µm
σ_k/k	$< 1.8\%$
f	> 0.44 mm
p	> 935

Table 3: Proposition for a set of parameters for hard X-rays for the vertical plane

Let it be supposed that this energy of 20.6 keV is too high for a certain design of the extraction mirror, the monochromator, the colloidal particles or the scintillator. Like it was initially proposed in the FCC-ee design report, in the case for a radiation with $\lambda = 1$ Å, that means an energy of approximately 12.4 keV the measurement can be performed for the following parameters in table 4. Again the camera should be able to resolve the fringe at two sigma of the decay due to spatial coherence with 10 pixels.

parameter	value
σ_y	15 µm
λ	$1 \cdot 10^{-10}$ m
z_1	100 m
z_2	5 m
a	< 1.5 µm
σ_k/k	$< 1.1\%$
f	> 0.75 mm
p	> 1643

Table 4: Proposition for a set of parameters for medium X-rays for the vertical plane

In general, it can be stated, that higher energies allow a monochromator with a broader bandwidth, a smaller sensor size, less pixels and smaller distances z_2. The disadvantage of higher energies is the smaller light yield in monochromator, colloids and scintillator, as harder X-rays interfere less with matter.

Horizontal Plane The beam is much wider in the horizontal plane (the mean width between the set measurement boundaries is $\sigma_x = 105$ µm), where another set parameters is ideal. First, ideal parameters for the horizontal plane are examined, so that later a set for both planes can be found, as measuring both the horizontal and the vertical beam size in one measurements is the ultimate goal.

For the small beam size in the vertical plane, there was the challenge that the fringes oscillate very fast. There the goal was to minimise the oscillation frequency of the fringes by maximising the energy and z_2. If one tries those parameters from the vertical plane for the horizontal plane, there would not be a single fringe visible. Therefore the challenge for the horizontal plane is to see at least some fringes, which occur for lower energies and smaller z_2. For those parameters, smaller colloids are needed.

An ideal set of parameters is given in table 5.

parameter	value
σ_x	105 µm
λ	$1 \cdot 10^{-10}$ m
z_1	100 m
z_2	0.2 m
a	< 0.4 µm
σ_k/k	$< 2.3\%$
f	> 0.1 mm
p	> 686

Table 5: Proposition for a set of parameters for medium X-rays for the horizontal plane

It can be seen, that for the horizontal plane and its big beam size, much less pixel are needed for an ideal set of parameters. The only disadvantages is, that the magnification has to be higher in order to have a field of view of $f = 0.1$ mm.

Both planes In order to find a trade off between the small wavelengths λ and the big distances z_2 for the vertical plane and the big wavelengths and the small distances for the horizontal plane, one has to cut back the expectations on the visible range of the decay due to limited spatial coherence. The goal is to be able to make a good resolution for a the average beam sizes of $\sigma_x = 15$ µm and for $\sigma_y = 105$ µm at the same time.

The following optimisation is therefore done with two further constraints. For the horizontal plane there shall be at least two fringes within the decay of two $\sigma_{vcz,x,q}$. This is set as the minimal tolerable condition to fit a Gaussian on the remaining Talbot oscillations to measure the beam size. For the vertical plane at least one $\sigma_{vcz,x,q}$ shall be resolved with 5 pixels. With those two conditions a setting is found in table 6, which needs the least amount of pixels.

For the upcoming simulation a wavelength of $\lambda = 1$ Å is chosen, as this is a good trade off between the refractive index and the intensity of the synchrotron radiation.

parameter	value
σ_x	105 µm
σ_y	15 µm
λ	$1 \cdot 10^{-10}$ m
z_1	100 m
z_2	3 m
a	< 1 µm
σ_k/k	$< 0.7\%$
f	> 0.75 mm
p	> 2600

Table 6: Proposition for a set of parameters for the both planes

5 Simulation

5.1 Numerical Proof of the Applicability of the Van Cittert Zernike Theorem

The essential assumption of this thesis is, that the radiation coming from an FCC-ee dipole holds true for the applicability of the Van Cittert Zernike theorem. In order to proof this, many wavefronts are going to be calculated with help of SRW. The initial positions of electrons are going to be randomly distributed on a Gaussian shape according to the actual transverse beam profile. For each colloid positions, its respective wavefront is calculated and stored in a file with index i.

In a second step the auto correlation function is going to be evaluated with all those wavefronts. This auto correlation function is expected to match the analytic prediction of the Van Cittert Zernike theorem.

The processing of wavefronts can be done sequentially, without having all of them in the memory at the same time. The spatial coherence is calculated using the following statement.

$$\Gamma = \frac{\left|\sum_{i=0}^{N} E_i \cdot E_i^*\right|}{\sum_{i=0}^{N} |E_i|^2} \tag{104}$$

For the sake of numerical efficiency and as long as the beam is symmetric along the x and the y axis, the simulation is done twice. First the electrons are distributed along x fixing there vertical position at $y = 0$ in Fig. 12 and then the other way round in Fig. 13. This can be done without loss of generality.

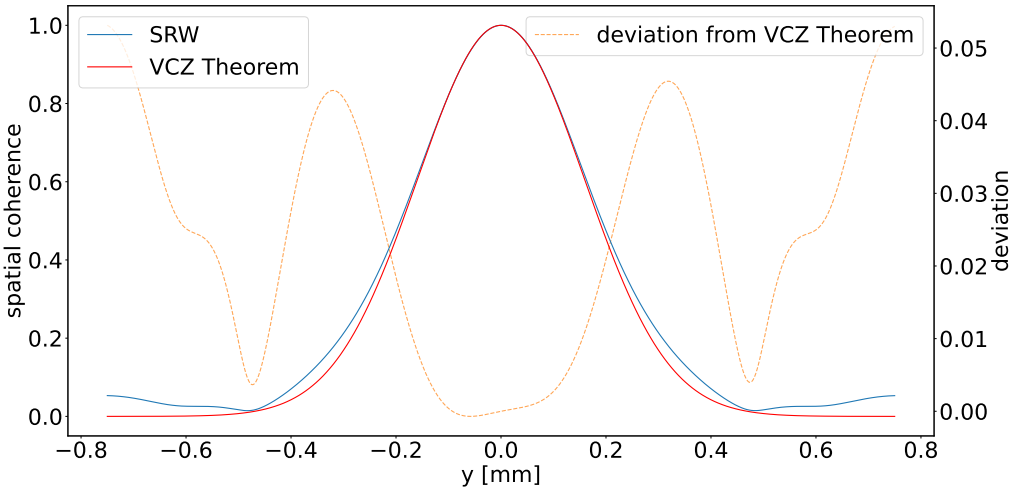

Figure 12: On the left y-axis the vertical coherence is shown, calculated with SRW. On the right y-axis one can see the deviation of this simulated coherence from the predicted coherence by means of the Van Cittert Zernike Theorem

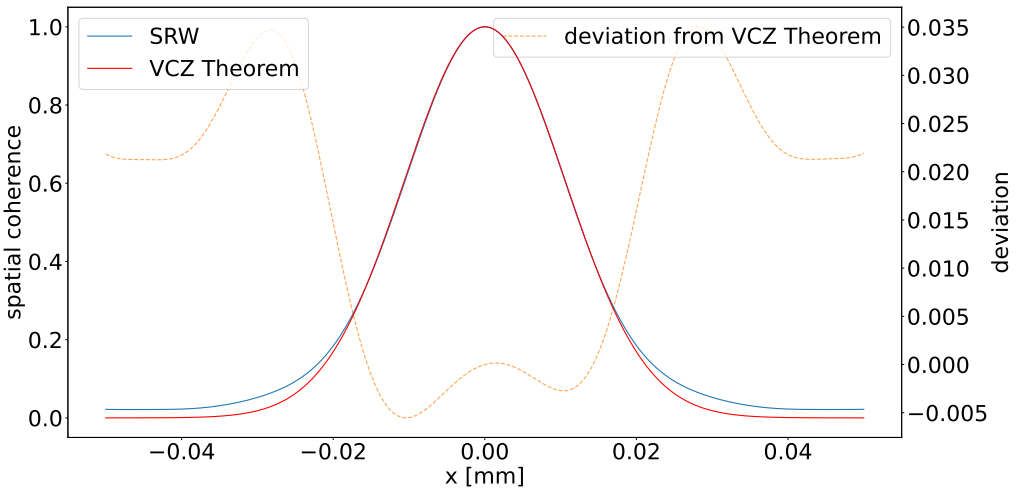

Figure 13: On the left y-axis the horizontal coherence is shown, calculated with SRW. On the right y-axis one can see the deviation of this simulated coherence from the predicted coherence by means of the Van Cittert Zernike Theorem

The result of the comparison between the Van Cittert Zernike Theorem and the

simulation for an FCC-ee arcdipole shows, that there are no significant deviations from the predicted full width at half maximum of the coherence area. Nevertheless fluctuations can be observed in the outer regions in the grid.

5.2 Simulating the Proposed Measurement

5.2.1 Structure of the simulation

First, an ensemble of N colloids is randomly distributed on transverse positions $c_i = (c_{x,i}, c_{y,i})$ in the distance $z = z_1$ downstream the magnet. Secondly, electrons are distributed on transverse positions $e_j = (e_{x,j}, e_{y,j})$ on a Gaussian shape according to the actual size of the beam of σ_x and σ_y at the centre of the sagittal coordinates at $z = 0$. Each colloid is going to emit radiation of a certain wavelength. Those photon energies have a centre wavevector k in addition to a normal distribution with a deviation σ_k. The fact, that each electron emits just one photon energy is by far not physical, but it turns out that the convergence is even faster in that setup.

Now for each electron with $e_j = (e_{x,j}, e_{y,j}, k_j)$, SRW calculates a wavefront at the position of the virtual image $z = z_1 + z_2 = z_3$, where z_1 is the distance between the source electrons and the colloids and z_2 is the distance between the colloid and the virtual image. Having calculated this wavefront each colloid emits a spherical wave, which amplitude is shaped by the function of the anomalous diffraction and which phase is tuned to be in phase with the SRW wavefront as described in (9).

Then all the electric fields of all the colloids waves and the electric field calculated by SRW are summed up, and the square of the absolute value is taken. In that case, the electric fields and not the intensities have to be added, because the synchrotron radiation produced by a single electron is fully coherent. This map of intensity is then stored.

This process is repeated for all electrons e_j and all their emitted energies. In a final step, all the intensities are summed up and processed in a 2D Fourier transform. Here the intensities and not the electric fields have to be summed up, as the synchrotron radiation of one electron is not coherent with the radiation of another electron.

The code is provided as a pseudo algorithm for a distributed computing cluster in algorithm (1). The SRW calculation has been prepared for parallel computing, by splitting the grid into smaller sections and calculating each of the independently on one processing unit.

```
define magnetic field/magnetic core length/magnetic soft edge/bending
 radius/energy of the electron beam/extension and position of the grid;
initialise electrons with x,y-position and emitting energy;
initialise scattering particles with x,y-positions;
split electrons in batches for all distributed computers in the batch cluster;
for all distributed computers do
    initialise zero valued intensity array I;
    for all electrons in the batch do
        initialise zeros valued electric field array E; calculated the electric field
         E_SRW of the synchrotron radiation with SRW;
        E = E + E_SRW;
        for all scattering particles do
            calculate the electric field of a spherical wave E_SCAT;
            calculate the phase for E_SCAT, so that there is no phase lag, between
             the synchrotron radiation and the spherical wave;
            calculate the scattering amplitude function for E_SCAT, that is the
             angular distribution of amplitude of the spherical wave;
            E = E + E_SCAT;
        end
        I = I + |E|^2
    end
end
collect and add intensities from all distributed computers;
2D Fourier transformation of I;
radial average of the transformation;
comparison with analytic predictions;
```

Algorithm 1: Algorithm of the simulation of a speckle pattern for measuring the spatial coherence of synchrotron radiation

5.2.2 Initialisation of the simulation

The first step is the magnetic structure of the dipole. For a preset of a class for long dipoles the code takes four arguments:

1. magnetic field $B = 14.1$ mT
2. magnetic core length $L_{core} = 23.94$ m
3. magnetic soft edge[5] $L_{soft} = 0.1$ m

[5]The soft edge is defined as the distance where the magnetic field drops to $1/e$ of its initial value. The given value is a guess, given the diameter of the beam pipe within the magnet of about 84mm. However this value does not have a significant influence, as the region of SR, which is observed is set to be the centre of the magnet and not its edges.

4. bending radius $\rho = 10760$ m

Secondly the initial position and energy of the particle passing through the dipole shall be set. The electron is supposed to go in perfectly straight right in the centre.

1. $x_0 = y_0 = z_0 = x'_0 = y'_0 = 0$
2. $\gamma = \frac{45600 \text{ MeV}}{0.510 \text{ MeV}} = 89411$

Thirdly, one has to choose at which position and on which mesh the synchrotron radiation is to be calculated. Furthermore the frequency of radiation, which is wished to be observed, has to be defined. Finally one can set a few precision parameter and optimisation strategies for the computation.

The output contains the full complex and two dimensional electric field in a given distance from the dipole.

5.2.3 Computational challenge

The main challenge of simulating the scattering of colloids is the amount of data being processed. To create a realistic wavefront, one has to simulate enough particles, so that the shape of its coherence converges to the predicted solution. For all of those particles there have to be enough variations of the observed frequencies, so that its temporal coherence converges towards to predicted function. In addition to that, each of those particle and each of its energy representations scatters independently at a few thousand colloids each, in order to create a realistic speckle pattern.

The simulation was tested on $16-core$ local workstation and then finally performed on CERN's HTCondor Cluster [6] where the simulated was deployed to several hundred cores.

5.3 Result of the simulation

The simulation has been performed with the proposed parameters from table 7.

[6] The HTCondor Cluster is a distributed high-throughput computing system, where calculations can be split to be performed on several of individual machines.

parameter	value
λ	$1 \cdot 10^{-10}$ m
z_1	100 m
z_2	3 m
a	0.5 µm
σ_k/k	0.1%
f	0.75 mm
p	= 2048
number of electrons	2000
number of colloids	1000

Table 7: Set of parameters for the main simulation

In Fig. 14 the two-dimensional Fourier transformation of the speckle pattern is plotted. The difference between the extent of the beam size of the horizontal and of the vertical plane is in evidence. Any patterns except the expected concentric fringes are not physical but optical illuding Moiré patterns and they tend to vanish, when zooming in or increasing the resolution of the grid.

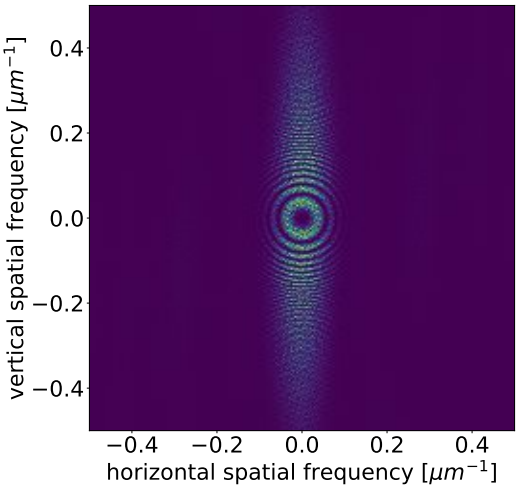

Figure 14: 2D Fourier transformation of the speckles simulation of the FCC-ee setup

5.3.1 Horizontal Plane

In Fig. 15 the radial (angular sectoral) average of the square of the absolute value of the 2D Fourier transformation of the simulated speckles pattern between 350°..10°/170°..190° is plotted. This double cone represents the horizontal plane. A total of four additional curves in addition to the actual result are plotted. There is

the curve of the decay of visibility of fringes only due to temporal coherence, only due to the finite angular distribution of the scattered intensity, only due to spatial coherence and finally the convolution of all contributing effects.

As foreseen in the theoretical treatment, only very few fringes are visible, due to the wide beam size in the horizontal plane of $\sigma_x = 105$ µm. This wide beam size transforms into a small coherence area, which stays small in the Fourier transformation.

The error of the fitted curve, compared to the predicted curve is: $\sigma_{fit}/\sigma_{total} - 1 = 1.5\%$

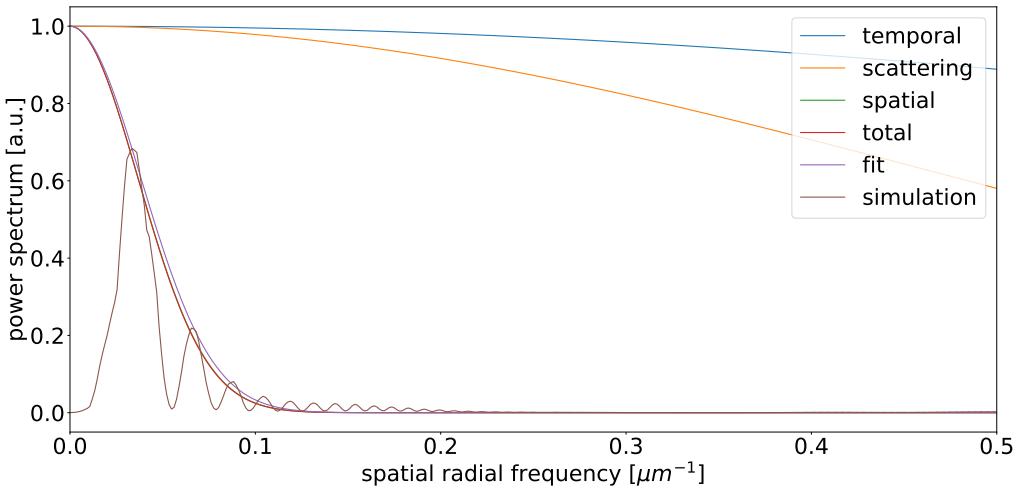

Figure 15: Horizontal cut of the 2D Fourier transformation of the speckles simulation of the FCC-ee setup

5.3.2 Vertical Plane

In Fig. 16 the radial (angular sectoral) average of the square of the absolute value of the 2D Fourier transformation of the simulated speckles pattern between 80°..100°/260°..280° is plotted. This double cone represents the vertical plane. Again a total of four additional curves in addition to the actual result are plotted as in the previous section.

As predicted in the theoretical treatment, very many fast oscillating fringes are visible, which are by theory guaranteed to be resolved properly until the first sigma of the total decay of visibility. Due to the small beam size in the vertical plane of $\sigma_y = 15$ µm, a very broad coherence area is obtained from the speckle pattern.

All frequencies above a certain threshold are cut of, as the maximal resolvable

frequency in a Fourier transformation is by definition $px/ext/2 \approx 0.7$. The error of the fitted curve, compared to the predicted curve is: $\sigma_{fit}/\sigma_{total} - 1 = 4.4\%$

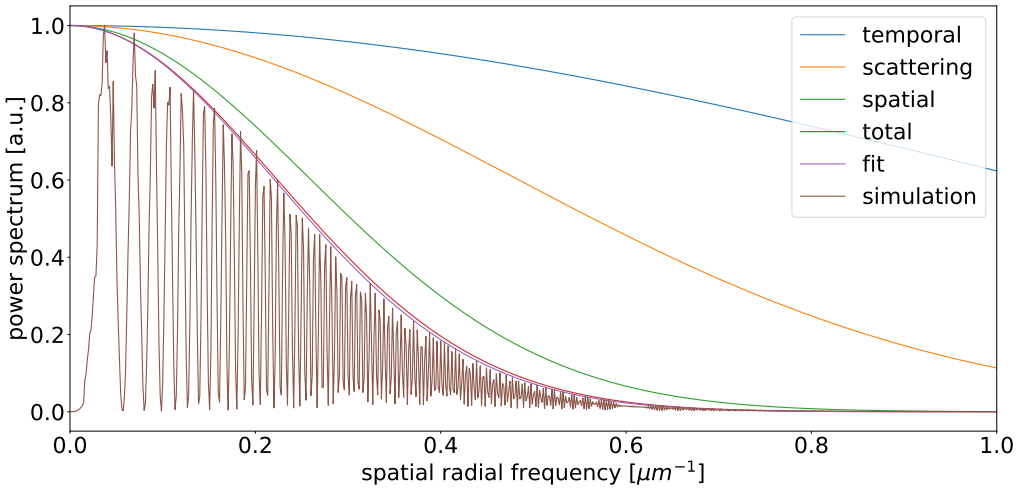

Figure 16: Vertical cut of the 2D Fourier transformation of the speckles simulation of the FCC-ee setup

5.3.3 Comments

The measurement of both dimensions of the beam size in one setup involves several challenges, as described in the theoretical section when optimising for a good set of parameters and as seen in the actual simulation. The resolution would be significantly increased, if it was possible to measure the vertical plane a few meters further downstream than the horizontal plane. For such a setup, the synchrotron radiation would have to be split into two separate beams. This can possibly be achieved by arranging two scintillators and tilted mirrors in the X-ray path as shown in Fig. 17.

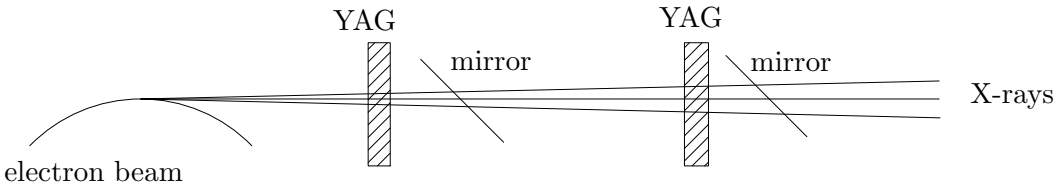

Figure 17: A proposal for measuring the speckle pattern at two different distances for increasing the resolution for each plane. The X-rays create a visible light image in the first YAG-scintillator on the left side, which is close to source. This distance is ideal for measuring the spatial coherence of the vertical plane. The X-rays would than pass through the mirror and create a second visible light image in the second YAG-scintillator. At those bigger distance the horizontal spatial frequency can be measured with higher accuracy.

6 Measurement of the Modulation Transfer Function

The key challenges of the measurement of the predicted speckle pattern are the conversion to visible light and the projection of the fringes on a sensor. Those two steps contribute to a certain transfer function, transferring the X-ray speckles to binary data.

The bottleneck of this overall transfer function is considered to be the modulation transfer function of the optical system and the magnification being used. This function describes, how well certain spatial frequencies are resolved by the optical apparatus.

The transfer function of an aberration-free diffraction-limited optical system can be calculated analytically and it depends on the numerical aperture, the working wavelength and on the coherence properties of the light being imaged. Many authors call this transfer function (taking in to account intermediate states of coherence) apparent transfer function (ATF) [36][37][15][38] or generalised transfer function (GTF) [39]. Having physically unavoidable optical aberrations due to imperfections of the system and other deviation from the predictions of paraxial optics, is leading to an additional suppression.

Despite the fact that the radiation has a certain amount of coherence, the imaging is going to take place with incoherent light, as all coherence properties are expected to vanish during to conversion to visible light. The idea of this chapter is to find the transfer function of this incoherent imaging system. For incoherent imaging this function is usually called the optical transfer function (OTF) and in case phase effects can be neglected it becomes the modulation transfer function (MTF). The problem is that this MTF is measured with methods, where sharp edges are going to be used to test the resolution of certain frequencies. The frequencies in speckles pattern are more sophisticated and are going to resemble squared sine function. This is why the transfer function is also going to be measured with colloids with coherent light, which is than mathematically transformed to an incoherent MTF. For that, the setup is placed under a condition, where there is no decay neither due to partial coherent light nor due to a non flat scattering amplitude function. The only decay which is going to be visible is due to the aberration and diffraction limited optics. The transfer function for coherent imaging is usually called the amplitude transfer function (ATF). This is because imaging with coherent light leads to a situation, where the system is not linear in the intensity but linear in the complex amplitude.

Summary of the Terminology In view of the many different partly identical terms used in literature and in the following chapters, a summary of all relevant transfer functions is listed here.

1. **GTF (ATF)** The generalised transfer function (or sometimes referred to as the apparent transfer function) is often defined via the relation between the power spectrum in the object and the power spectrum in the image plane. This type of function is used for all different coherent properties [15][39].

2. **PSF** The point spread function is the optical response to a point. The PSF of a microscope is the Airy function.

3. **ESF** The edge spread function is an image taken of a sharp edge, which depicts the transition from a transparent to an opaque area [40].

4. **LSF** The line spread function is the derivation of the ESF, which resembles the optical response to a mathematical line. This is similar to the optical response to a point (point spread function) [40].

5. **OTF** The optical transfer function is the Fourier transformation of the LSF [40].

6. **MTF** The modulation transfer function is the absolute value of the complex valued OTF [40].

7. **ATF** The amplitude transfer function is the common term for a transfer function when dealing with coherent light [41].

6.1 Incoherent MTF

6.1.1 Visibility of Linepairs

A very straightforward method to measure the spatial resolution of an optical system is to take images of pairs of lines. For an imaginary perfect optical system the contrast between the black and white areas is perfect for all frequencies of line pairs. For a real optical system at some point the black and white areas are going to blur into grey. The contrast between the maximum intensities of the black areas and the minimum intensities of the white areas is defined with help of the interferometric visibility.

$$V = \frac{I_{max} - I_{min}}{I_{max} + I_{min}} \tag{105}$$

The function of those visibilities for different frequencies of line pairs is a way to depict the MTF.

If there is a series of maxima $I_{max,i}$ and minima $I_{min,i}$ in a comb of those pairs of lines, a good way to measures the visibility is to take the average of all maxima and all minima. The average of all extrema is denoted by μ.

$$V = \frac{\frac{1}{N}\sum_{i=1}^{N} I_{max,i} - \frac{1}{N}\sum_{i=1}^{N} I_{min,i}}{\frac{1}{N}\sum_{i=1}^{N} I_{max,i} + \frac{1}{N}\sum_{i=1}^{N} I_{min,i}} = \frac{\frac{1}{N}\sum_{i=1}^{N} I_{max,i} - I_{min,i}}{2\mu} \tag{106}$$

The operation can be rearranged in terms of a non squared, but absolute valued standard deviation

$$\mu = \frac{1}{N} \sum_{i=1}^{N} I_{max,i} + I_{min,i} \tag{107}$$

$$\sigma = \sum_{i=1}^{N} |\mu - I_{max,i} - I_{min,i}| \tag{108}$$

For a perfect visibility the comb of linepairs has infinitely sharp edges, which is why all the values of the measured intensities are either a maximum or a minimum. In theory the average of intensities of linepairs is always 0.5 because, exactly half the light passes through.

For a rough estimation it is reasonable to calculate the non squared standard deviation for all intensities. This holds true perfect visibility and no visibility and the region within is approximated to be linear in this estimation.

6.1.2 Slant Edge

Another more sophisticated, but widely used way of measuring the MTF of an optical system is the so-called slant edge method.

A slant edge MTF target is a glass with a transparent and a non transparent side, whose edge between white and black is slightly slanted. A standard angle of this slanted line is 4 degrees.

If a picture is taken of this glass plate, most pixels will see either black or white, but some, which are looking at the edge, will receive a partly black partly white window and return a grey level. Then all pixels of the image are projected on a straight line, which is normal on the tilted edge as drawn in Fig. 18. This projection is the edge spread function (ESF). The derivation of the ESF is the so-called line spread function (LSF). The Fourier transform of this LSF is the OTF and its absolute value the MTF [40].

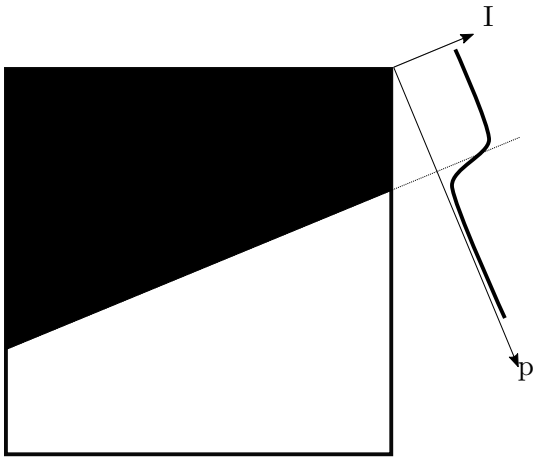

Figure 18: Schematic explanation of the slanted edge method

6.1.3 Analytic Treatment

For diffraction-limited aberration-free optical system with incoherent light, the MTF can be easily evaluated analytically. A cutoff frequency is defined [41].

$$q_0 = \frac{NA}{\lambda} \tag{109}$$

For imaging with incoherent light, the MTF expands up to $2 \cdot q_0$. With the spatial frequency q this decay is given in [41].

$$\mathcal{MTF}(q) = \begin{cases} \frac{\pi}{2}\left(\arccos\left(\frac{q}{2q_o}\right) - \frac{q}{2q_o} \cdot \sqrt{1-\left(\frac{q}{2q_o}\right)^2}\right) & q \leq 2q_0 \\ 0 & \text{else} \end{cases} \tag{110}$$

6.1.4 Summary

The method of imaging linepairs and the one using a slanted edge have been performed with a 20x microscope objective with an numerical aperture of NA=0.4. Those MTFs were then compared to the analytic prediction of a diffraction limited system according to (110) in Fig. 19. The deviation of the measured MTF from the prediction is then given by any kinds of optical aberrations.

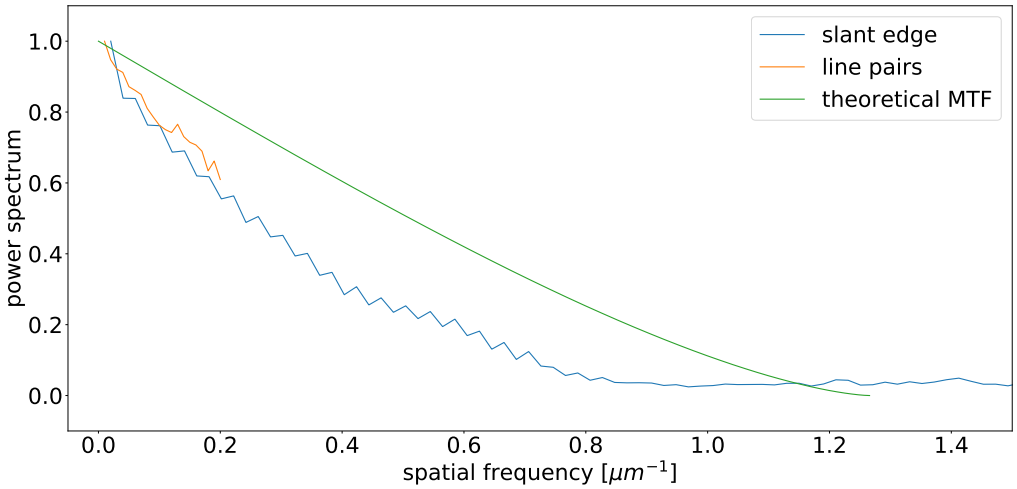

Figure 19: Different methods for the evaluation of the MTF compared with the theoretical diffraction-limited prediction with a 20x and NA=0.4 microscope

The MTF measured with linepairs stop at q=0.2µm. This is because the thinnest pairs of lines, which were available have 200 lines per millimetre.

6.2 Coherent ATF

6.2.1 Setup of the Experiment

The methods for determining the modulation transfer function for incoherent light sources described in the previous chapter are all well known in the field of optics. The technique to measure the ATF, that is the GTF for coherent light relies on a novel approach using colloids.

A spatial filtered laser is used, to have a clean Gaussian intensity profile with no higher fluctuations and to have a temporally and spatially fully coherent beam. Furthermore, colloids are used which are so small, that they scatter with a flat scattering amplitude function in the region of interest. Hence one should see fringes, which are only suppressed by the limited optical resolution.

The whole setup for measuring the ATF is shown in Fig. 20.

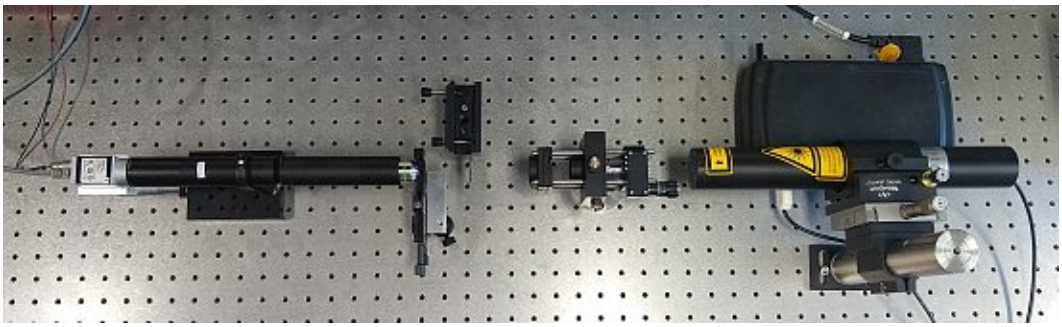

Figure 20: Lab setup for measuring the ATF

First, the laser beam is spatially filtered with a 20 µm pinhole. If the beam was big enough, this would not be necessary. As the used laser produces a spot size, which would be to small for the measurement one has to magnify it. By magnifying, fluctuations and disturbances are introduces, wherefore it is useful the magnify and filter spatially in one step. The spatial filtering has been tested for two different pinhole diameters in Fig. 21.

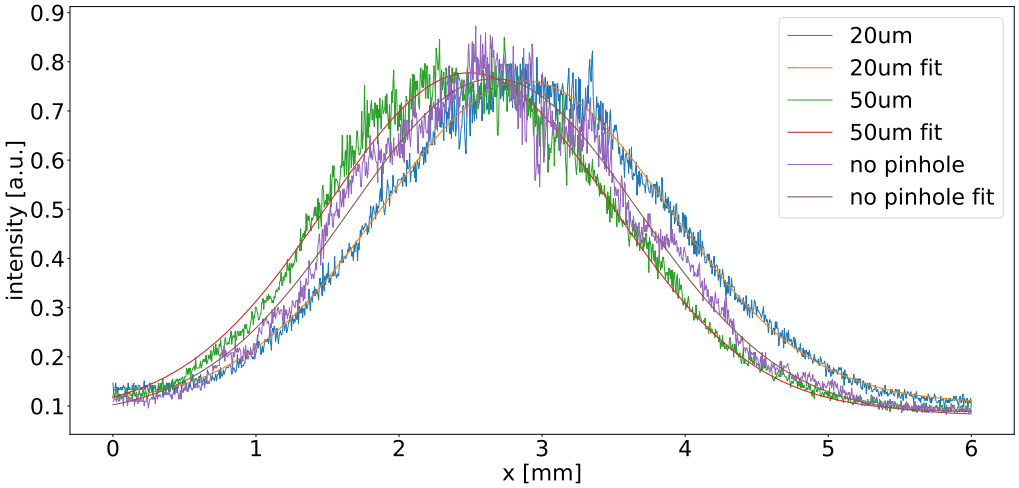

Figure 21: Effect of the spatial filtering for different pinhole sizes

Secondly, the laser passes trough a 10% neutral density filter, as the beam would saturate the used sensor even for the shortest exposure time of 25 µs.

Thirdly, the beam drifts through a cuvette with a thickness of 1 mm, holding the spherical nanoparticles in a liquid suspension. The calculation for the density of the colloids is performed in the next chapter 6.2.2.

Finally, a virtual image is generated at the desired distance and projected onto the sensor via a microscope lens (20x or 10x) in combination with a $f = 200$ mm tube lens.

The camera which was used, is a Basler acA1600-20gm with the following specifications.

parameter	values
Resolution (H x V)	1626 px x 1236 px
Pixel Size (H x V)	4.4 µm x 4.4 µm
EMVA Quantum Efficiency (typical)	46.4
Signal-to-Noise Ratio (typical)	39.2 dB
Dark Noise (typical)	9.4 e^-
Pixel Bit Depth	12 bits

Table 8: Specifications of the Basler acA1600-20gm

6.2.2 Density of Colloids

As described in the introduction, the Heterodyne Near Field Speckles relies on having a strong transmitted and a relatively weak scattered radiation. In general the technique works for the scattered intensity being about 10% of the transmitted intensity.

In order to find the right density of colloids in a cuvette of thickness d, one has to calculate the exstinction cross section of the colloids. This is done with the help of the Mie theory [21] and especially with the formula (71). For colloids with a radius of $a = 500$ nm and a refractive index for a working wavelength of $\lambda = 632$ nm of $n = 1.457/1.333$ the extinction cross section is $C_{ext} = 3.3 \cdot 10^{-13}$ m^2. Here the relative refractive index of silica in water is used.

Introducing ρ, the density of particles per unit volume, the intensity of the transmitting beam after a distance x within a colloidal suspension is

$$I(x) = I_0 \cdot \exp\left(-n \cdot C_{ext} \cdot x\right) \tag{111}$$

In order to achieve $I(d) = 0.9 \cdot I_0$ the density of colloids shall be

$$\rho = \frac{-\ln(0.9)}{C_{ext} \cdot d} = 3 \cdot 10^{14} \mathrm{m}^{-3} \tag{112}$$

An indication in volume proportions is easier to handle. With the total volume V_{total}, and the volume of all the colloids V_{coll}.

$$\frac{V_{coll}}{V_{total}} = \frac{4\pi a^3}{3} \cdot \rho = \frac{1}{6340} \tag{113}$$

The silica colloids by Sigma Aldrich were delivered in a 10% suspension. That means that this solutions has to be diluted in a ratio of 1:634 with distilled water.

6.2.3 Experiment

A python script was written to perform live analysis during the measurement. The program continuously streams data from the camera and calculates the average of a certain amount of recent images. Then this static background is subtracted from the most recent image, resulting in a pure speckle pattern as seen in Fig. 22.

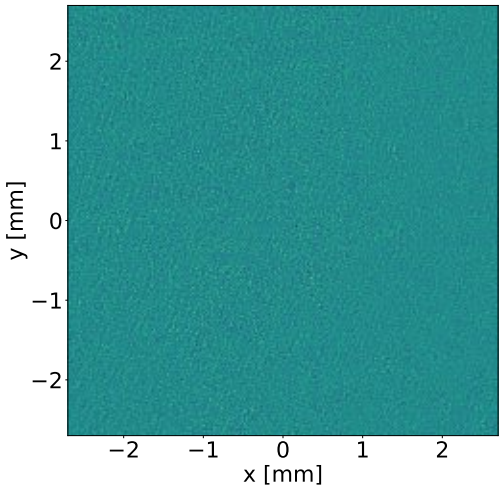

Figure 22: A typical speckle pattern, where the background has been subtracted

Then a two-dimensional Fourier transformation is performed on this image. The script now takes a few of those recent Fourier transformations, averages them and computes the radial average.

As imposed by the design of this setup all frequencies up the cutoff frequency (109) should be distributed equally in the speckle pattern in Fig. 22. The diffraction-limited aberration-free ATF is calculated to be the following Heaviside function [41].

$$ATF(q) = H(q - q_0) \tag{114}$$

This cutoff is clearly obvious in the power spectrum of the speckle pattern [7]. In addition to that diffraction-limited sharp cutoff a slow additional decay is visible,

[7] Given the earlier theoretical treatment one should expect Talbot oscillations to be visible. In this case they are too fast to be resolved leading to a situation where only their mean values are visible. This is commonly referred to as the shadowgraph signal.

which relates to the aberration-limited part. Figure 23 shows this measurement for a 10x microscope with an numerical aperture of NA=0.25 for two different colloid types with radii $r = 1$ µm and $r = 0.5$ µm. Two different radii were chosen for improved universality of the result.

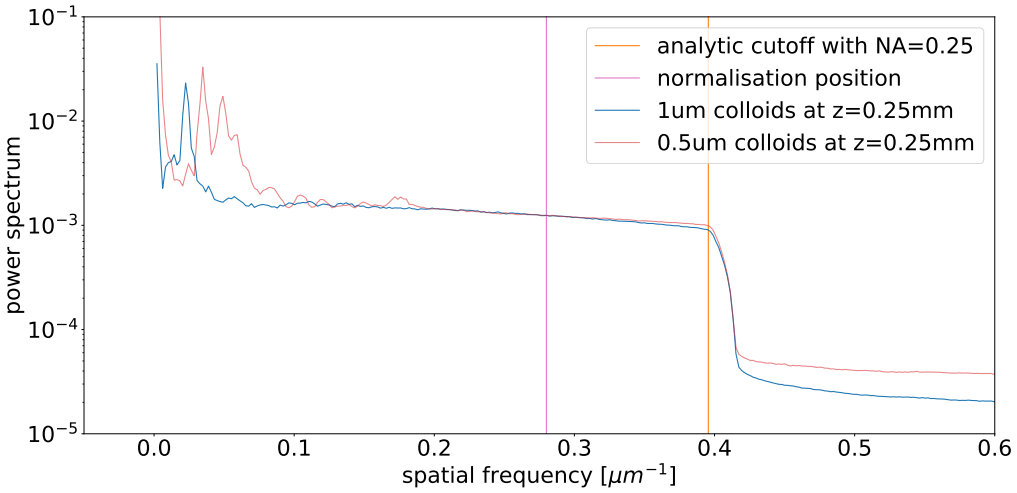

Figure 23: ATF measured with the diffraction at colloids compared with the theoretical diffraction-limited prediction with a 10x microscope and two different colloids size. The normalisation of both curves is done at $q = 0.28$ µm^{-1}.

6.3 Comparison of MTF and ATF

When correcting the MTFs measured with incoherent light by the theoretical predicted diffraction-limited decay (110), both strategies match until the cutoff of the ATF in (114) [8]. Those functions then resemble the decay, which is only due to aberrational effects. This proves that measuring the MTF with standard methods is also valid for the peculiarities of measuring the power spectrum of a speckle pattern. This comparison is plotted in Fig. 24 for a 20x microscope with an numerical aperture of $NA = 0.4$.

[8] In principle the ATF refers to the transferred amplitude and the MTF to the transferred intensity. This is because for coherent images complex values of the electric fields have to be added while for the incoherent illumination, intensities are added, because phase effects become irrelevant in the time average over the statistical fluctuations of incoherent light. This means that imaging with coherent light, implies that the optical system is nonlinear in the intensity. Due to due fact that the ATF is rectangular function, squaring would not have an effect on the shape, which is why both methods can be compared in this way.

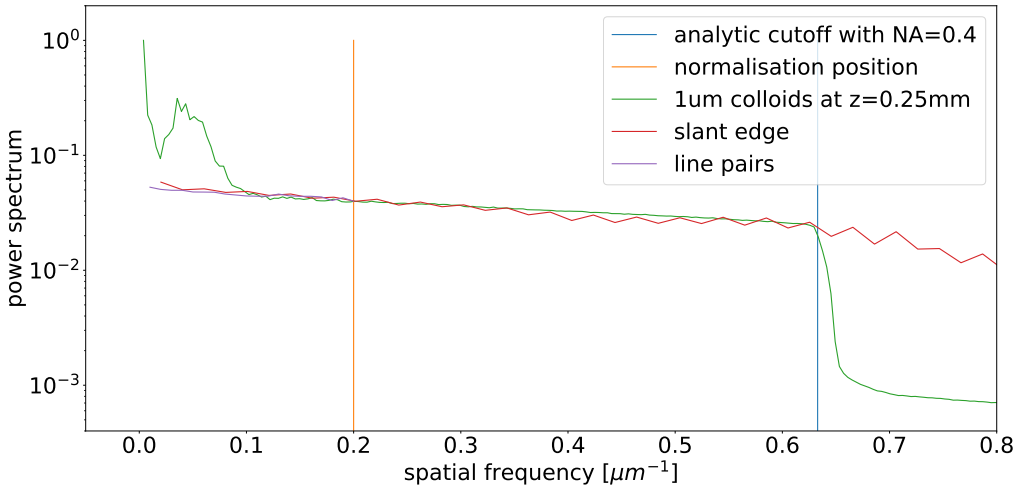

Figure 24: The measurements of the diffraction corrected MTFs compared with the measurement of the ATF performed with a 20x microscope. The normalisation is done at $q = 0.2$ µm^{-1}

When performing the proposed technique to monitor the beam size at FCC-ee, the MTF has to be measured precisely in order to correct the simulated power spectrum of the speckle pattern by this calibration curve.

In general it can be seen that the power spectrum of a speckle pattern without any imposed decay, is sufficiently flat for higher frequencies but lacks flatness especially for low frequencies up to q=0.1 µm^{-1}. This could have an serious impact on the resolution of the beam size in the horizontal plane. To overcome those limitations two separate setups for each plane could be used as mentioned earlier.

7 Conclusion

It has been shown, that the synchrotron radiation of the magnetic structure of an FCC-ee arc bending dipole, which is generated at the energies foreseen by the design study, can be used to calculate the transverse beam size from the radiation's spatial coherence. It has been further proven, that for a certain set of parameters of the optical beam lines devices - which are the extraction windows, the monochromator, the properties of the colloidal suspension, the scintillator and the optical system - a interferogram can be produced, which reveals information about the spatial coherence and as a further consequence of the transverse beam size.

In summary, this technique is in principle suitable for determining the transverse beam size at the FCC-ee on a bunch-per-bunch basis and it is feasible with actual technology. For a more reliant application in the FCC tunnel further studies should take place, finding solid materials which are capable of replacing the rather fragile installation of the colloidal suspension and studying possibilities of separating the measurement for each plane individually.

List of Figures

List of Tables

References

[1] Marzio Giglio et al. "Near-field intensity correlations of scattered light". In: *Appl. Opt.* 40.24 (Aug. 2001), pp. 4036–4040. DOI: 10.1364/AO.40.004036.

[2] Doriano Brogioli, Alberto Vailati, and Marzio Giglio. "Heterodyne near-field scattering". In: *Applied Physics Letters* 81.22 (2002), pp. 4109–4111. DOI: 10.1063/1.1524702.

[3] M. D. Alaimo et al. "Probing the Transverse Coherence of an Undulator X-Ray Beam Using Brownian Particles". In: *Phys. Rev. Lett.* 103 (19 Nov. 2009), p. 194805. DOI: 10.1103/PhysRevLett.103.194805.

[4] M. Siano et al. "Characterizing temporal coherence of visible synchrotron radiation with heterodyne near field speckles". In: *Phys. Rev. Accel. Beams* 20 (11 Nov. 2017), p. 110702. DOI: 10.1103/PhysRevAccelBeams.20.110702.

[5] M. Siano et al. "Electron size measurements using the heterodyne near field speckles at ALBA". In: *Transverse profile and emittance monitors*. 8th International Beam Instrumentation Conference. Malmö (Sweden): JACoW Publishing, 2019, pp. 383–386. DOI: 10.18429/JACoW-IBIC2019-TUPP031.

[6] *European Strategy Particles Physics Update 2013*. https://cds.cern.ch/record/1567258/files/esc-e-106.pdf. Accessed: 2020-05-07.

[7] A. Abada, M. Abbrescia, and S.S. AbdusSalam. "FCC-ee: The Lepton Collider". In: *Eur. Phys. J. Spec. Top* 228 (2019), p. 388. DOI: 10.1140/epjst/e2019-900045-4.

[8] *Die Nord-Süd-Achse Gotthard*. https://company.sbb.ch/de/medien/dossier-medienschaffende/weitere-dossiers/gotthard-basistunnel.html. Accessed: 2020-05-07.

[9] John David Jackson. *Classical electrodynamics*. 3rd ed. New York, NY: Wiley, 1999. ISBN: 9780471309321.

[10] Enrico Bravin. "Transverse Emittance Measurement". In: *Cern Accelerator School on Beam Instrumentation*. 2018.

[11] K. Desler and D.A. Edwards. "Accelerator physics of colliders". In: *European Physics Journal* 15 (2000), pp. 157–159. DOI: 10.1007/BF02683417.

[12] J. Emery et al. "A fast and accurate wire scanner instrument for the CERN accelerators to cope with severe environmental constraints and an increased demand for availability". In: *2014 IEEE Conference on Control Applications (CCA)*. 2014, pp. 1139–1145.

[13] *Secondary emission monitor (SEM) grids*. http://cds.cern.ch/record/43009?ln=de. Accessed: 2020-05-07.

[14] Daniele Butti. "Synchrotron radiation interferometry for beam size measurement in the large hadron collider". PhD thesis. Politecnico di Milano, 2019.

[15] Joseph W Goodman. *Statistical Optics*. Vol. 1. John Wiley & Sons, New York, NY, 2015.

[16] O. Chubar and P. Elleaume. "Accurate And Efficient Computation Of Synchrotron Radiation In The Near Field Region". In: *proc. of the EPAC98 Conference* (June 1998), pp. 1177–1179.

[17] G. Trad et al. "A novel approach to synchrotron radiation simulation". In: *IPAC 2014: Proceedings of the 5th International Particle Accelerator Conference* (July 2014), pp. 3687–3689.

[18] O. Chubar, P. Elleaume, and A. Snigirev. "Phase analysis and focusing of synchrotron radiation". In: *Nuclear Instruments and Methods in Physics Research Section A: Accelerators, Spectrometers, Detectors and Associated Equipment* 435 (1999), pp. 495–508. DOI: 10.1016/S0168-9002(99)00581-1.

[19] G. Geloni, E. Saldin, and E. Schneidmiller. "Fourier Optics treatment of Classical Relativistic Electrodynamics". In: *Deutsches Elektronen-Synchrotron DESY Hamburg* (2006). URL: arXiv:physics/0608145.

[20] H.C. Hulst. *Light Scattering by Small Particles*. Structure of matter series. Wiley, 1957.

[21] Wolfram Hergert and Thomas Wriedt. "Basics and Applications". In: *The Mie Theory*. Springer-Verlag Berlin Heidelberg, 2012. Chap. 3, p. 73. ISBN: 978-3-642-28737-4. DOI: 10.1007/978-3-642-28738-1.

[22] Craig F. Bohren and Donald R. Huffman. "Appendixes: Computer Programs". In: *Absorption and Scattering of Light by Small Particles*. Wiley, 2007, pp. 475–476. ISBN: 9783527618156. DOI: 10.1002/9783527618156.app1.

[23] Amos Egel et al. “CELES: CUDA-accelerated simulation of electromagnetic scattering by large ensembles of spheres”. In: *Journal of Quantitative Spectroscopy and Radiative Transfer* 199 (2017), pp. 103–110. ISSN: 0022-4073. DOI: 10.1016/j.jqsrt.2017.05.010.

[24] F. Zernike. “The concept of degree of coherence and its application to optical problems”. In: *Physica* 5.8 (1938), pp. 785–795. ISSN: 0031-8914. DOI: 10.1016/S0031-8914(38)80203-2.

[25] Max Born et al. “Interference and diffraction with partially coherent light”. In: *Principles of Optics: Electromagnetic Theory of Propagation, Interference and Diffraction of Light*. 7th ed. Cambridge University Press, 1999, pp. 554–632. DOI: 10.1017/CBO9781139644181.019.

[26] A. Khintchine. “Korrelationstheorie der stationären stochastischen Prozesse”. In: *Mathematische Annalen* (1934), pp. 604–615.

[27] J.C. Dainty. *Laser Speckle and Related Phenomena* -. Berlin Heidelberg: Springer Science & Business Media, 2013. ISBN: 978-3-662-43205-1.

[28] Philip Willmott. *An introduction to synchrotron radiation: techniques and applications; 2nd ed.* Chichester: John Wiley & Sons, Apr. 2019. DOI: 1119280397.

[29] Carolyn MacDonald. *An introduction to X-ray physics, optics, and applications*. Princeton, NJ: Princeton University Press, 2017.

[30] Y Shvyd’ko. *X-Ray Optics*. Berlin, Heidelberg: Springer, 2004. Chap. High-Resolution X-Ray Monochromators. DOI: 10.1007/978-3-540-40890-1.

[31] Shigemitsu Nakanishi and Tetsuo Horiguchi. “Surface Lattice Constants of Si(111), Ni(111) and Cu(111)”. In: *Japanese Journal of Applied Physics* 20.3 (Mar. 1981), pp. L214–L216. DOI: 10.1143/jjap.20.l214. URL: https://doi.org/10.11432Fjjap.20.l214.

[32] T. Martin, A. Koch, and M. Nikl. “Scintillator materials for x-ray detectors and beam monitors”. In: *MRS Bulletin* 42.6 (2017), pp. 451–457. DOI: 10.1557/mrs.2017.116.

[33] Marco Stampanoni et al. “High resolution X-ray detector for synchrotron-based microtomography”. In: *Nucl. Instrum. Meth. A* 491 (Sept. 2002), pp. 291–301. DOI: 10.1016/S0168-9002(02)01167-1.

[34] H. H. Hopkins and Cecil Reginald Burch. “The frequency response of a defocused optical system”. In: *Proceedings of the Royal Society of London. Series A. Mathematical and Physical Sciences* 231.1184 (1955), pp. 91–103. DOI: 10.1098/rspa.1955.0158.

[35] *YAG:Ce scintillations properties. CRYTUR, spol. s r.o. Na Lukách 2283 51101 Turnov Czech Republic*. http://www.crytur.com/materials/yagce. Accessed: 2020-05-07.

[36] H. H. Hopkins. “Applications of Coherence Theory in Microscopy and Interferometry”. In: *J. Opt. Soc. Am.* 47.6 (June 1957), pp. 508–526. DOI: 10.1364/JOSA.47.000508.

[37] Richard J. Becherer and George B. Parrent. “Nonlinearity in Optical Imaging Systems”. In: *J. Opt. Soc. Am.* 57.12 (Dec. 1967), pp. 1479–1486. DOI: 10.1364/JOSA.57.001479.

[38] S. L. Zhuang and F. T. S. Yu. “Apparent transfer function for partially coherent optical information processing”. In: *Applied Physics B* 28.28 (Aug. 1982), pp. 359–366. DOI: 10.1007/BF00686367.

[39] Yobani Mejía and David E.G. Suárez. “Optical transfer function with partially coherent monochromatic illumination”. In: *international Journal for Light and Electron Optics* 193.163021 (Sept. 2019). DOI: 10.1016/j.ijleo.2019.163021.

[40] Xujie Zhang et al. “Measuring the modulation transfer function of image capture devices: what do the numbers really mean?” In: *Image Quality and System Performance IX*. Ed. by Frans Gaykema and Peter D. Burns. Vol. 8293. International Society for Optics and Photonics. SPIE, 2012, pp. 64–74. DOI: 10.1117/12.912989.

[41] Joseph W Goodman. *Introduction to Fourier optics*. 3rd ed. John Wiley & Sons, New York, NY, 2005.